AN ALTERNATIVE APPROACH TO MEASURING REVERBERATION LAGS IN ACTIVE GALACTIC NUCLEI

YING ZU,[1] C.S. KOCHANEK,[1,2] AND BRADLEY M. PETERSON[1,2]
Draft version May 3, 2011

ABSTRACT

Motivated by recent progress in the statistical modeling of quasar variability, we develop a new approach to measuring emission-line reverberation lags to estimate the size of broad-line regions (BLRs) in active galactic nuclei. Assuming that all emission-line light curves are scaled, smoothed, and displaced versions of the continuum, this alternative approach fits the light curves directly using a damped random walk model and aligns them to recover the time lag and its statistical confidence limits. We introduce the mathematical formalism of this approach and demonstrate its ability to cope with some of the problems for traditional methods, such as irregular sampling, correlated errors, and seasonal gaps. We redetermine the lags for 87 emission lines in 31 quasars and reassess the BLR size–luminosity relationship using 60 Hβ lags. We confirm the general results from the traditional cross-correlation methods, with a few exceptions. Our method, however, also supports a broad range of extensions. In particular, it can simultaneously fit multiple lines and continuum light curves which improves the lag estimate for the lines and provides estimates of the error correlations between them. Determining these correlations is of particular importance for interpreting emission-line velocity–delay maps. We can also include parameters for luminosity-dependent lags or line responses. We use this to detect the scaling of the BLR size with continuum luminosity in NGC 5548.

Subject headings: galaxies: active — galaxies: nuclei — galaxies: Seyfert — quasars: general

1. INTRODUCTION

While it is widely accepted that the enormous luminosities of active galactic nuclei (AGNs) are attributable to accretion of matter onto supermassive black holes (BH), detailed studies are extremely challenging on account of the small angular scales of the regions involved in the accretion process. Direct probes of the sub-microarcsecond structure of AGNs has been therefore limited to VLBI studies of the radio-emitting regions, gravitational microlensing studies of the accretion disk (see review by Wambsganss 2006) and reverberation mapping of the broad-line regions (Blandford & McKee 1982; Peterson 1993). The technique of reverberation mapping (a.k.a. echo mapping) exploits the light travel time between the central engine and the broad-line region (BLR) to deduce the structure of the BLR (see Peterson 2001 for a tutorial). The continuum radiation from the accretion disk photoionizes gas clouds near the AGN to produce broad emission lines, thus encoding the geometry and kinematics of the clouds (Osterbrock 1989; Peterson 1997; Krolik 1999). The physical *ansatz* for reverberation mapping is straightforward:

1. The continuum emission of the quasar shows (stochastic) variability that drives emission-line variations after a light travel-time delay.

2. The unobservable ionizing UV continuum that drives the emission lines is simply related to the observable satellite UV or optical continuum (i.e.,

the pattern and phase of variations are closely correlated).

3. The light-travel time is the most important time scale; specifically, the local emission-line response time to continuum changes is assumed to be instantaneous and the dynamical time scale of the BLR is much larger than the light-travel time across it.

The relationship between the observables, continuum light curve $s_c(t)$ and the emission-line light curve $s_l(t, V)$ where V is the line-of-sight velocity, is taken to be

$$s_l(t, V) = \int d\tau \, \Psi(\tau, V) s_c(t - \tau), \tag{1}$$

where $\Psi(\tau, V)$ is known as the "transfer function" or "velocity–delay map." In reality, the relationship between the continuum and emission-line variations can be non-linear, but the amplitude of variation on reverberation time scales is sufficiently small that the linear approximation seems to be justified. Inspection of Equation (1) shows that $\Psi(\tau, V)$ is the observed response of the broad emission-line region to a delta-function continuum outburst, mapped into the observable quantities time delay τ and line-of-sight velocity V. The data requirements for successful recovery of the transfer function are quite demanding (Horne et al. 2004) and consequently most efforts to date have concentrated on measuring only the *total* emission-line response to continuum variations. The transfer equation (eq. 1) then becomes

$$s_l(t) = \int d\tau \, \Psi(\tau) s_c(t - \tau), \tag{2}$$

where $\Psi(t) = \int \Psi(\tau, V) \, dV$ is variously known as the "one-dimensional transfer function" (so that $\Psi(t, V)$ is

[1] Department of Astronomy, The Ohio State University, 140 West 18th Avenue, Columbus, OH 43210; yingzu@astronomy.ohio-state.edu.
[2] Center for Cosmology and AstroParticle Physics, The Ohio State University, 191 West Woodruff Avenue, Columbus, OH 43210

the "two-dimensional transfer function" or the "delay map"). For the remainder of this paper, we will refer to $\Psi(t)$ simply as the "transfer function." In most investigations to date, it is the mean response time or "lag" $\langle\tau\rangle$ that one tries to measure, generally by cross-correlation of the continuum and emission-line light curves, as we discuss further below. The importance of measuring the emission-line lag is two-fold: first, $\langle\tau\rangle$ yields a characteristic physical scale for emission of a particular line, $R = c\langle\tau\rangle$, and this can be combined with some measure of the emission-line Doppler width ΔV to obtain an estimate of the central black hole mass. Assuming that gravity is the dominant force on the line-emitting gas, the virial equation for the central black hole mass is

$$M_{\rm BH} = \frac{f\Delta V^2 R}{G}, \qquad (3)$$

where G is the gravitational constant and f is a dimensionless factor of order unity that depends on the geometry, velocity field, and inclination of the BLR. We note in passing that there is currently an active debate about the relative importance of radiation pressure on the BLR gas and how this affects reverberation-based mass measurements (Marconi et al. 2008; Netzer 2009; Marconi et al. 2009; Netzer & Marziani 2010). While the possible role of radiation pressure in measurement of black hole masses is an important issue, it has no direct bearing on the present discussion, which is about measuring time delays. Similarly, there is still active discussion about the mean value of the scaling factor $\langle f\rangle$ (e.g., Onken et al. 2004; Labita et al. 2006; Woo et al. 2010; Graham et al. 2011) that is beyond the scope of this contribution. Second, reverberation studies have established a tight empirical relationship between the BLR size and the AGN continuum luminosity (Kaspi et al. 1996; Kaspi et al. 2000, 2005; Bentz et al. 2006, 2009) that allows us to use the luminosity as a surrogate for the BLR size in eq. (3) and thus estimate the masses of black holes in AGNs from individual spectra (Wandel et al. 1999; Vestergaard 2002; McLure & Jarvis 2002, 2004; Vestergaard & Peterson 2006; Kollmeier et al. 2006; Shen et al. 2008). This allows us to explore BH properties and evolution with redshift (e.g., Kollmeier et al. 2006; Peng et al. 2006; Hopkins & Hernquist 2006; Shankar et al. 2009; Steinhardt & Elvis 2010; Kelly et al. 2010), thus providing valuable insights into the mystery of black hole growth and its connection to galaxy evolution at high redshift, where the quasar population is evolving dramatically. The potential for obtaining simple estimates for the masses of black holes in quasars provide a means of exploring the correlations between the BH mass and global properties of their host galaxies such as the bulge luminosity ($M_{\rm BH}$–$L_{\rm bulge}$ relationship; Kormendy & Richstone 1995; Magorrian et al. 1998; Bentz et al. 2009) and bulge stellar velocity dispersion ($M_{\rm BH}$–$\sigma_\star$ relationship; Ferrarese & Merritt 2000 Gebhardt et al. 2000a,b; Tremaine et al. 2002; Ferrarese et al. 2001; Onken et al. 2004; Nelson et al. 2004; Gültekin et al. 2009) both locally and potentially over cosmic time.

As a practical problem in aperiodic time-series data analysis, reverberation mapping requires high-fidelity spectroscopic monitoring of the continuum and emission-

line variations for a duration long compared to the emission-line lag (Horne et al. 2004), which is observed to range from hours to a year or more, depending on the luminosity of the AGN and the cosmic time dilation at its redshift. Emission-line lags have been measured for more than three dozen AGNs by cross correlation of the continuum and emission-line light curves. The particular challenge of dealing with reverberation time series is that they are generally irregularly sampled for various reasons, including unfavorable weather and, for higher-luminosity objects with larger lags, annual conjunctions with Sun that cause seasonal gaps in the observed time series. In practice, two methodologies have been widely employed to deal with unevenly sampled data. The first method is to interpolate between real data points to obtain a regular sampling grid for computation of the cross-correlation function (CCF) as a function of time delay τ (Gaskell & Sparke 1986; Gaskell & Peterson 1987; White & Peterson 1994; Peterson et al. 1998; Welsh 1999; Peterson et al. 2004). The second method, the discrete correlation function (DCF) method (Edelson & Krolik 1988), bins the data over discrete time intervals on which the data are reasonably well-sampled and a correlation coefficient is computed for the time delays between each pair of continuum/emission-line time bins. A variant on this is the Z-transformed DCF (Alexander 1997) which varies the width of the time bins to better distribute the data points among the time bins. White & Peterson (1994) show that when common assumptions and normalizations are used, the interpolation CCF method and the DCF method give similar results. However, as the time-sampling becomes sparser, the interpolation method significantly outperforms the DCF method as long as interpolation of the light curves (usually linear in practice) remains a reasonable assumption[3].

Presumably even more accurate lags could be measured given more realistic modeling of the continuum behavior between real measurements of the continuum and emission-line fluxes. This now seems to be a real possibility given the recent work of Kelly et al. (2009), who find that quasar variability can be well described by a damped random walk. By applying the variability model to the light curves of known quasars and comparing them to other variable sources, Kozłowski et al. (2010) show that quasars occupy a very distinctive region in the model parameter space of time scale and variability amplitude. MacLeod et al. (2010) then apply the model to $\sim 9{,}000$ spectroscopically identified quasars in SDSS Stripe 82. They confirm that the model can de-

---

[3] Consider, as an example, the UV and optical monitioring campaign on NGC 5548 undertaken with the *International Ultraviolet Explorer* (Clavel et al. 1991) and ground-based telescopes (Peterson et al. 1991) in 1989. The UV data were sampled at approximately regular 4-day intervals. Analysis of these data using the interpolation CCF (Peterson & Wandel 1999) revealed for the first time a "virial relationship" between the emission-line lags and line widths (i.e., $\langle\tau\rangle \propto \Delta V^{-2}$), thus providing an empirical justification for using Equation (3) to estimate the black hole mass. Analysis of these same data with the DCF method (Krolik et al. 1991) obscured this result at least in part because of "discretization noise" introduced by the DCF: because of the regular 4-day sampling, the smallest usable time bin for the DCF was also four days, resulting in lag measurements that were integer multiples of 4 days, significantly reducing the time resolution of the lag measurements and smearing out the $\langle\tau\rangle$–ΔV anticorrelation.

scribe quasar variability well and they explore the correlation of the variability parameters with other properties of quasars such as wavelength, luminosity, BH mass, and Eddington ratios in detail. Importantly for reverberation studies, the formalism is able to statistically predict the value of light curve at an unmeasured time based on the overall statistical properties of the light curve. It provides a well-defined statistical model for interpolating light curves and can do appropriate statistical averages over the uncertainties in the model predictions.

Given a complete statistical framework for describing the continuum variability, and the overall *ansatz* that emission-line variability is a scaled and smoothed version of the continuum, we can build an alternative approach to measuring reverberation lags, aspects of which were previously noted by Rybicki & Kleyna (1994). Among the advantages of this approach are:

1. It not only interpolates between data points, but also self-consistently estimates and includes the uncertainties in the interpolation.

2. It can separate light curve means, trends, and systematic errors in flux calibration from variability signals and meansurement noise in a self-consistent way.

3. Correlated errors can be treated naturally.

4. Lags of multiple emission lines and their covariances can be derived simultaneously.

5. It provides statistical confidence limits on the lag estimates as well as other parameters.

We describe the methodology of our approach in detail in §2. In §3, we present the statistical process model for the continuum light curves. We briefly describe our data set and apply this method to the estimate of Hβ lags in §4. We further show how the method can address the problem of correlated errors in §5 and how it can be used to improve lag estimates, particularly in the presence of seasonal gaps, by fitting multiple lines simultaneously in §6. We also fit the $R_{\mathrm{BLR}}-L$ relationship using Hβ lags determined by our method in §7. In §8, we add a luminosity dependence to the lag and solve for the lag–luminosity relationship of NGC 5548. We summarize our main findings and discuss future applications and expansions of our approach in §9.

2. METHODOLOGY

Press et al. (1992) and Rybicki & Press (1992) developed a method to statistically analyze irregularly sampled light curves, and Rybicki & Kleyna (1994) applied the variant we now consider to four seasons of optical reverberation data on NGC 5548. Here we reintroduce this approach, which we have named "Stochastic Process Estimation for AGN Reverberation (SPEAR[4])," with several modest changes in algorithm and a broad range of new applications.

Except for the transfer function $\Psi(\tau)$, our notation is chosen for comparison with Rybicki & Kleyna (1994).

[4] http://www.astronomy.ohio-state.edu/~yingzu/spear.html

We start with a model process driving the continuum $s_c(t)$ that has a covariance between times t_i and t_j of

$$\langle s_c(t_i)s_c(t_j)\rangle = \sigma^2 \exp(-|t_i - t_j|/\tau_{\mathrm{d}}). \qquad (4)$$

We adopt here an exponential covariance matrix for concreteness, since we know from Kelly et al. (2009), Kozłowski et al. (2010) and MacLeod et al. (2010) that quasar light curves are well modeled by this process. Physically, the model corresponds to a random walk described by an amplitude $\sigma^2 = \hat{\sigma}^2\tau_{\mathrm{d}}/2$ on long time scales and an exponential damping time scale τ_{d}, where $\hat{\sigma}$ and τ_{d} are used as our model parameters. Rybicki & Press (1992) estimated the covariance matrix based on the structure function of the continuum light curve, while here we adopt a specific parametrized model that will be optimized as part of the analysis.

Slightly rewriting Equation (2) for convenience and to facilitate comparison with Rybicki & Kleyna (1994), the light curve of a line is

$$s_l(t) \equiv \int dt' \Psi(t - t')s_c(t). \qquad (5)$$

Since the lines and continuum are related by the transfer function, we can also determine the covariance between the line and continuum

$$\langle s_l(t_i)s_c(t_j)\rangle = \int dt' \Psi(t_i - t')\langle s_c(t')s_c(t_j)\rangle, \qquad (6)$$

between the line and itself

$$\langle s_l(t_i)s_l(t_j)\rangle = \int dt'dt'' \Psi(t_i - t')\Psi(t_j - t'')\langle s_c(t')s_c(t'')\rangle, \qquad (7)$$

and between two different lines

$$\langle s_l(t_i)s_l'(t_j)\rangle = \int dt'dt'' \Psi(t_i - t')\Psi'(t_j - t'')\langle s_c(t')s_c(t'')\rangle. \qquad (8)$$

If the light curve of the line is divided into velocity bins δV, then there is a transfer function for each bin $\Psi(t - t', V)$ and we can compute all the expected covariances between the light curves. For convenience, let **s** be a vector comprised of all the light curves, both line and continuum, and $S = \langle \mathbf{ss}\rangle$ be the covariance matrix between all the elements of **s**. By definition, in Gaussian statistics the probability of the light curve is simply

$$P(\mathbf{s}) \propto |S|^{-1/2} \exp\left(-\frac{\mathbf{s}^T S^{-1}\mathbf{s}}{2}\right). \qquad (9)$$

We do not measure the actual light curve, but some realization of it, $\mathbf{y} = \mathbf{s} + \mathbf{n} + L\mathbf{q}$, in which there is measurement error **n**, whose probability distribution is

$$P(\mathbf{n}) \propto |N|^{-1/2} \exp\left(-\frac{\mathbf{n}^T N^{-1}\mathbf{n}}{2}\right). \qquad (10)$$

where $N = \langle \mathbf{nn}\rangle$ is the covariance matrix of the noise. Note that nothing requires N to be diagonal, so there is no formal difficulty to including covariances in the noise between the line and continuum.

In defining **y**, we have also allowed for the simultaneous fitting of a general trend defined by a response matrix L and a set of linear coefficients **q**. In particular, we use this to fit and remove separate means from the light curves.
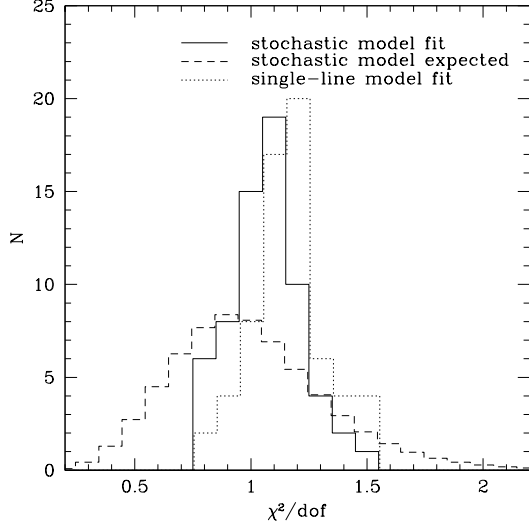
FIG. 1.— Distribution of χ^2 per degree of freedom for the continuum fits. The solid histogram is the χ^2/dof distribution of our stochastic model, while the dashed one shows the distribution expected for models with correctly estimated Gaussian uncertainties. The dotted histogram is the χ^2/dof distribution of the joint model of the continuum and Hβ light curves from §4.

In this application to a model with two light curves, L is a $2 \times K$ matrix with entries of $(1,0)$ for the continuum data points and $(0,1)$ for the line data points, where K is the total number of data points. The linear parameters are a very general tool. For example, separate linear trends would be removed with a $4 \times K$ matrix with entries of $(1, t_i, 0, 0)$ for continuum epoch t_i and $(0, 0, 1, t_j)$ for line epoch t_j. Two sources of data with potentially different *but constant* levels of contamination from the host galaxy can be reconciled by using different means for each line and continuum data source, corresponding to a $4 \times K$ matrix with entries of $(1, 0, 0, 0)$ for the first continuum source, $(0, 1, 0, 0)$ for the second continuum source, $(0, 0, 1, 0)$ for the first line source and $(0, 0, 0, 1)$ for the second line source. Unlike current approaches focused on cross-correlation functions, the uncertainties in these linear parameters are fully incorporated into the uncertainties in any other parameter estimate.

Given these definitions, the probability of the data $\mathbf{y}$ given the linear coefficients $\mathbf{q}$, the intrinsic light curves $\mathbf{s}$, and any other parameters of the model $\mathbf{p}$ is

$$P\left(\mathbf{y}|\mathbf{q}, \mathbf{s}, \mathbf{p}\right) \propto |SN|^{-1/2}$$
$$\int d^n \mathbf{n} \, d^n \mathbf{s} \, \delta\left(\mathbf{y} - (\mathbf{s} + \mathbf{n} + L\mathbf{q})\right) \exp\left(-\frac{\mathbf{s}^T S^{-1} \mathbf{s} + \mathbf{n}^T N^{-1} \mathbf{n}}{2}\right). \tag{11}$$

After evaluating the Dirac delta function, we "complete the squares" in the exponential with respect to both the unknown intrinsic source variability $\mathbf{s}$ and the linear coefficients $\mathbf{q}$. This exercise determines our best estimate for the intrinsic variability

$$\hat{\mathbf{s}} = SC^{-1}(\mathbf{y} - L\hat{\mathbf{q}}) \tag{12}$$

and the linear coefficients

$$\hat{\mathbf{q}} = (L^T C^{-1} L)^{-1} L^T C^{-1} \mathbf{y} \equiv C_q L^T C^{-1} \mathbf{y} \tag{13}$$

where $C = S + N$ is the overall covariance matrix of the

data and $C_q = (L^T C^{-1} L)^{-1}$. With these definitions we can factor the argument of the exponential into

$$P\left(\mathbf{y}|\mathbf{q}, \mathbf{s}, \mathbf{p}\right) \propto |SN|^{-1/2}$$
$$\exp\left(-\frac{\mathbf{\Delta s}^T (S^{-1} + N^{-1})\mathbf{\Delta s}}{2} - \frac{\mathbf{\Delta q}^T C_q^{-1} \mathbf{\Delta q}}{2} - \frac{\mathbf{y}^T C_\perp^{-1} \mathbf{y}}{2}\right) \tag{14}$$

where

$$C_\perp^{-1} = C^{-1} - C^{-1} L C_q L^T C^{-1} \tag{15}$$

is the component of C that is orthogonal to the fitted linear functions, the variances in the linear parameters are

$$\langle \mathbf{\Delta q}^2 \rangle = (L^T C^{-1} L)^{-1} \equiv C_q, \tag{16}$$

$\mathbf{\Delta s} = \mathbf{s} - \hat{\mathbf{s}}$ and $\mathbf{\Delta q} = \mathbf{q} - \hat{\mathbf{q}}$. We can marginalize the probability over the light curve $\mathbf{s}$ and the linear parameters $\mathbf{q}$ under the assumption of uniform priors for these variables to find that

$$P\left(\mathbf{y}|\mathbf{p}\right) \propto \mathcal{L}$$
$$\equiv |S + N|^{-1/2} \left|L^T C^{-1} L\right|^{-1/2} \exp\left(-\frac{\mathbf{y}^T C_\perp^{-1} \mathbf{y}}{2}\right) \tag{17}$$

where $\mathcal{L}$ represents the likelihood function we are to maximize, and the remaining parameters $\mathbf{p}$ are those describing the process (Equation 4) and the transfer functions. The term in the exponent, $\mathbf{y}^T C_\perp^{-1} \mathbf{y}$, is the generalized χ^2 that we present throughout the paper. While this treatment of linear parameters was included by Rybicki & Press (1992), Rybicki & Kleyna (1994) chose to subtract fixed means rather than marginalizing over them as part of the analysis as we do here. The variance in the estimate for the mean light curve is

$$\langle \mathbf{\Delta s}^2 \rangle = S - S^T C_\perp S. \tag{18}$$

We can estimate the light curve $s(t)$ at any unmeasured time using the same formalism. The simplest means of doing so is simply to pad the data vector $\mathbf{y}_d$ with additional fake points $\mathbf{y}_f$ that have infinite measurement uncertainties in the sense that $N^{-1} \to 0$ for these points. After appropriately partitioning the matrices, the estimate of the light curve at the unmeasured points is

$$\hat{\mathbf{s}}_f = S_{fd}(S_{dd} + N_{dd})^{-1} \mathbf{y}_d \tag{19}$$

with variance relative to the true light curve of

$$\langle \mathbf{\Delta s}_f^2 \rangle = S_{ff} - S_{fd}(S_{dd} + N_{dd})^{-1} S_{df}. \tag{20}$$

where S_{dd}, S_{ff}, S_{fd} and S_{df} are the data-data, fake-fake, fake-data and data-fake covariance matrices of the process and N_{dd} is the noise matrix of the data. The inclusion of the fake points has no effect on the expected results for the measured data points.

Just to re-emphasize the point, this formalism was first outlined by Rybicki & Kleyna (1994) based on Press et al. (1992) and Rybicki & Press (1992). We have refined it slightly to use a specific process model, to optimize the parameters of that model and to include the means of the light curves as parameters that are automatically marginalized. Unfortunately, we will not be able to use the fast implementation of this method for
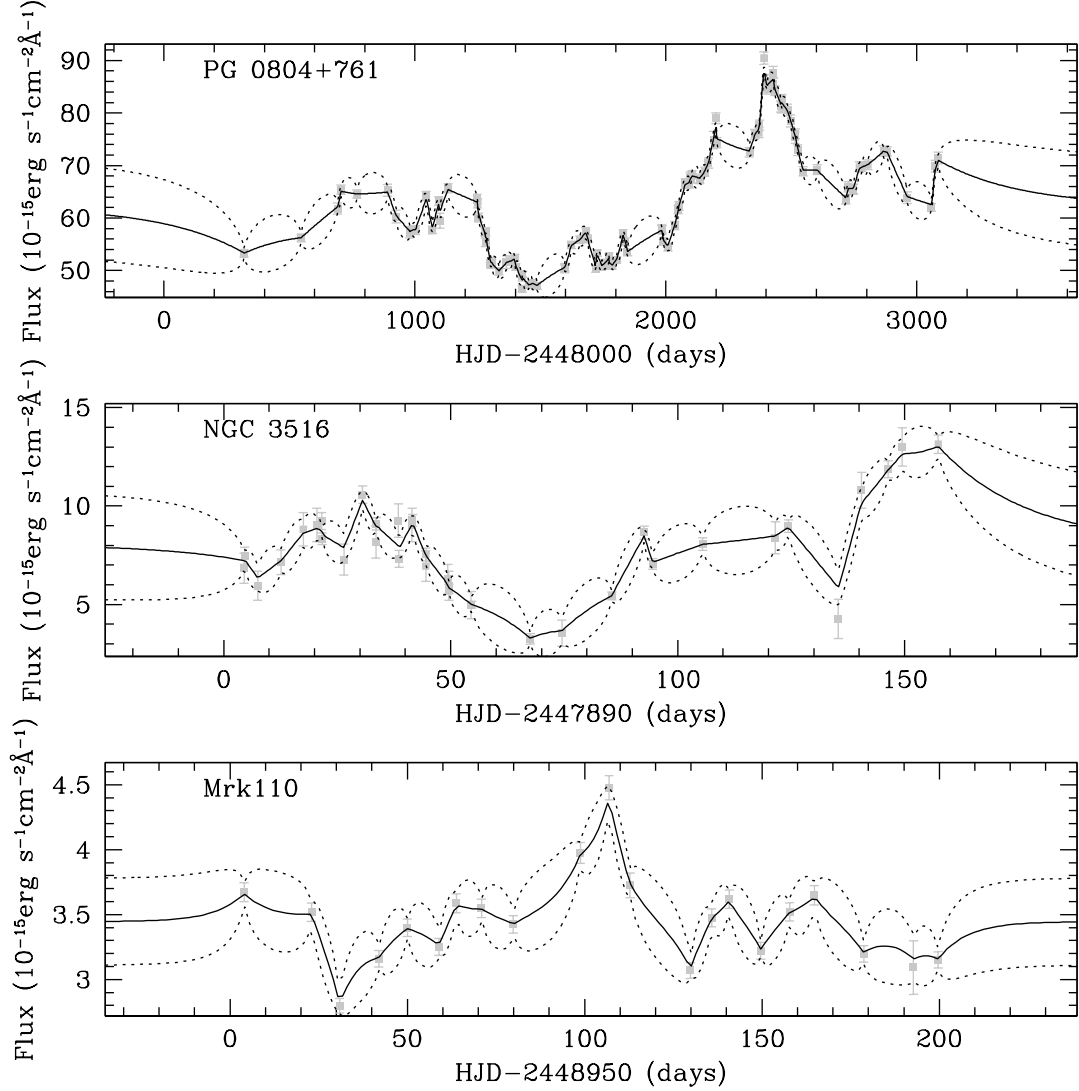
FIG. 2.— Continuum models. The solid line shows the expected mean source light curve $\hat{\mathbf{s}}$ (Equation 12) and the dashed line shows the expected spread (Equation 18) of light curves about the mean consistent with the data. An individual light curve realization consistent with the data (see Equation 21) will show more structure than this mean light curve and have excursions outside the dashed line consistent with the estimated variance.

exponential covariance matrices from Rybicki & Press (1995), because the inclusion of the transfer functions means that S is not a simple exponential covariance matrix and hence does not have a simple, tridiagonal inverse for the fast method.

We can, however, use the fast methods for generating simulated light curves. In particular, we are interested in light curves constrained to resemble the continuum light curve. As discussed by Rybicki & Press (1992), such a light curve is simply the estimated mean light curve given by Equation (12) with an added random component that has the covariance matrix $Q = (S^{-1} + N^{-1})^{-1}$. Rybicki & Press (1992) suggest determining the eigenmodes of Q which are then the independent "normal" modes that can be added to the mean light curve to produce a random realization constrained by the continuum light curve. This is computationally expensive. Instead, we note that if we Cholesky decompose $Q = M^T M$,

where M is an upper triangular matrix, and define the random component of the light curve by $\mathbf{u} = M\mathbf{r}$ where $\mathbf{r}$ is a vector of zero-mean, unit-dispersion Gaussian random deviates, that

$$\langle \mathbf{u}\mathbf{u}^T \rangle = M\langle \mathbf{r}\mathbf{r}^T \rangle M^T = MM^T = Q^T = Q \qquad (21)$$

since the covariance matrix $\langle \mathbf{r}\mathbf{r}^T \rangle$ of the Gaussian deviates is simply the identity matrix and Q is symmetric. Since Q^{-1} is a tridiagonal matrix given the exponential covariance matrix and a diagonal noise matrix, we can generate very high dimension $\mathbf{u}$ that can be convolved with the transfer function to produce a simulated line light curve in $\mathcal{O}(K)$ operations rather than the $\mathcal{O}(K^3)$ needed following the eigenmode approach.

The original application of the method by Press et al. (1992) was to cross correlate the light curves of two images of a lensed quasar in order to estimate the time delay between them. While this was not discussed in

terms of transfer functions, it does correspond to a trans-
fer function of the form $\Psi(t_i - t_j) = \delta(t_i - (t_j + \Delta t))$,
making the second light curve a lagged version of the
first. Press et al. (1992) also treated the parameters cor-
responding the process as fixed parameters, derived by
fitting a power law to the structure functions of the light
curve. It is likely that some combination of neglecting
uncertainties in the process model or covariances in the
errors of the light curves led Press et al. (1992) to ob-
tain an incorrect estimate of the time delay despite the
elegance of the approach.

In Rybicki & Kleyna's (1994) expansion of the method
to reverberation mapping, they used rising and falling
sawtooth and isosceles triangle transfer functions, finding
little difference between the results or ability to discrimi-
nate between them. Thus, for this initial reconnaissance,
we will simply use a top-hat (rectangular function) for
the transfer function,

$$\Psi(t - t') = A(t_2 - t_1)^{-1} \quad \text{for} \quad t_1 \leq t - t' \leq t_2 \quad (22)$$

which has a mean lag of $\langle \tau \rangle = (t_1 + t_2)/2$ and a temporal
width of $\Delta\tau = t_2 - t_1$. The necessary integrals for Equa-
tions (6), (7), and (8) are all analytic (see the Appendix)
and the model includes the limits of a delta function as
$\Delta\tau \to 0$ and a uniform thin shell as $t_1 \to 0$. The scal-
ing coefficient A determines the line response for a given
change in the continuum (i.e., the responsivity of BLR
clouds), but for present purposes we will largely view it
as a nuisance variable.

We use the *amoeba* minimization method (Press et al.
1992) to optimize the solution and then either a Monte
Carlo Markov Chain (MCMC, Metropolis et al. 1953;
Hastings 1970) or optimization over a grid to estimate
parameter uncertainties. We carry out the analysis in
two phases. We first analyze the continuum light curve
on its own, using logarithmic priors for τ_d and $\hat\sigma$ to deter-
mine the range of the variability process parameters con-
sistent with the continuum light curve. The logarithmic
prior on τ_d essentially penalizes values that deviate from
the median sampling intervals to avoid both unphysi-
cally large τ_d and a second class of solutions of $\tau_d \to 0$,
when all data are completely uncorrelated and the model
simply uses σ to broaden the uncertainties until obtain-
ing an acceptable fit. Then we do the joint analysis of
the continuum and the lines using Gaussian priors for τ_d
and $\hat\sigma$ determined from the analysis of the continuum in
isolation. In detail, we take the results of the MCMC
analysis of the continuum and used uncorrelated priors
on $\ln \tau_d$ and $\ln \hat\sigma$ (which is conservative), where the prior
for each variable was centered at the median value with
the Gaussian width chosen to match the upper and lower
1σ confidence regions. We then used uniform priors for
A, t_1 and t_2.

The reason for using the continuum to define a stronger
Gaussian prior on the process variable before carrying
out the joint analysis is to eliminate the aforementioned
second class of solutions of $\tau_d \to 0$ that could poten-
tially bias our lag estimates. This secondary solution
always exists at some level because of the finite temporal
sampling. For modeling the continuums, we are only an-
alyzing cases with significant variability, so this is not an
issue for the individual light curves. However, in the joint
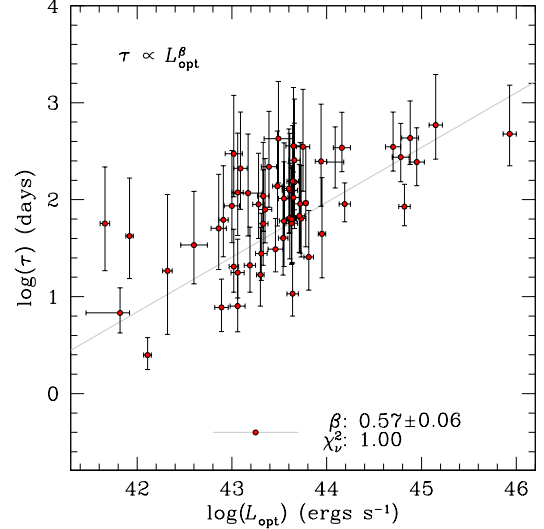analysis, if we fit the line and continuum light curves si-

Fig. 3.— Rest-frame damping timescale τ_d of the continuum light
curves as a function of optical luminosity. The uncertainties in τ_d
are the $\pm 1\sigma$ range.

multaneously at the wrong lag, the optimal solution will
be to let $\tau_d \to 0$ since there are then no correlations
between data points. Physically, it made more sense to
consider only the ranges for the process variables τ_d and
$\hat\sigma$ that were statistically consistent with the continuum
variability.

3. THE STATISTICAL PROCESS MODEL OF THE CONTINUUM

This approach depends on using a statistical model for
the variability process of the continuum in order to opti-
mally model the underlying light curve of the continuum.
Here we use the exponential covariance matrix suggested
by Kelly et al. (2009), although it was also introduced
by Rybicki & Press (1995) to enable a fast version of the
SPEAR approach. Physically, the exponential covariance
matrix in Equation 4 corresponds to a damped random
walk with an amplitude scale $\hat\sigma$ and a damping time scale
τ_d. On long time scales the variance of the light curve is
$\hat\sigma(\tau_d/2)^{1/2}$ and on short time scales it is $\hat\sigma\sqrt{t}$.

Kelly et al. (2009) use this to model the light curves
of 100 quasars, including some of the objects we will
consider here, using a light curve forecasting approach
to estimate the process parameters. Kozłowski et al.
(2010) show how the Kelly et al. (2009) approach can
be derived from the SPEAR approach and demonstrated
that forecasting is less statistically optimal for parame-
ter estimation than using the complete light curve mod-
eling method of SPEAR, and then applied the pro-
cess model and the SPEAR method to the OGLE-
III (Udalski et al. 2008) light curves of ~ 2500 mid-
infrared-selected quasars behind the Magellanic Clouds
(Kozłowski & Kochanek 2009). They confirm that
the damped random-walk model describes quasar light
curves well, and that quasars occupy a well-defined re-
gion of τ_d–$\hat\sigma$ parameter space. This is further confirmed
by MacLeod et al. (2010), who used this approach to
model 9,000 SDSS quasars to examine the correlations
of σ and τ_d with other quasar properties.

Unlike the previous papers, we fit flux rather than mag-
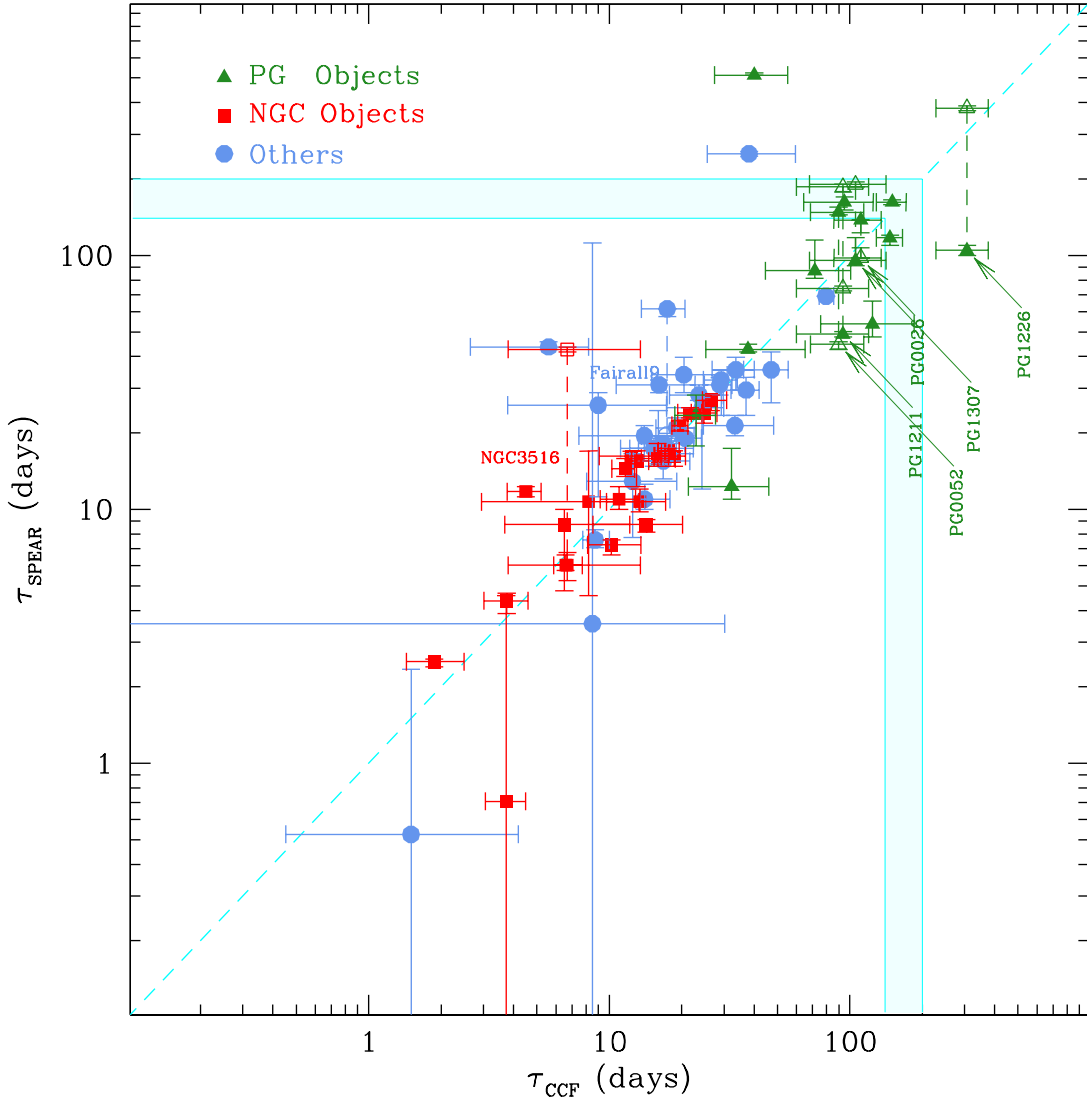nitude light curves because the line flux is more closely

FIG. 4.— Comparison of rest-frame Hβ time lags from the CCF and the SPEAR methods. Green triangles, red squares and blue circles were used for the PG, NGC and other objects, respectively, with $\pm 1\sigma$ error bars indicated on both estimates. The labeled points linked by dashed vertical lines are objects having multiple lag solutions and the filled symbol is the higher likelihood solution. The two intersecting stripes indicate the region where the solutions from *both* methods may be false due to the seasonal gap (140–200 days, with time dilation).

related to the continuum flux than to the continuum magnitude. Thus, we start by examining how well the damped random-walk process models the 60 continuum flux light curves for the 31 systems we consider in §4. Figure 1 shows the distribution of the χ^2 per degree of freedom for the best-fit models of all the continuum light curves we consider. Since half of the continuum light curves in our sample have less than 50 data points, the expected χ^2/dof distribution is broader than that of the OGLE light curves (~ 500 points) considered by Kozłowski et al. (2010). Nevertheless, the χ^2/dof distribution indicates that the statistical process model provides a reasonable fit to the light curves. The fact that the distribution is narrower than expected for correctly estimated Gaussian uncertainties suggests that the reported photometric errors are somewhat larger than the true uncertainties, or that there has been some pruning of outliers from the light curves.

Figure 2 shows three examples of modeled continuum light curves interpolated and extrapolated from Equation (12) and their uncertainties from Equation (18), as well as the observed light curve. The estimated light curve at time t is in essence a weighted average over data points within the damping time $|t - t'| \lesssim \tau_{\rm d}$ that balances the variance expected on those time scales due to the process against the uncertainties in the data point to determine how closely the model light curve approaches a particular data point. Far from any data points, the model returns to the light curve mean on the time scale $\tau_{\rm d}$. Remember, however, that Equation (12) is an estimate for the average of all possible light curves that could be drawn from the process that would be consistent with the data — a particular realization of such a light curve would show additional structure (see Rybicki & Press 1992). The "error snake" surrounding the model light curve is the variance in these possible light curves. Near
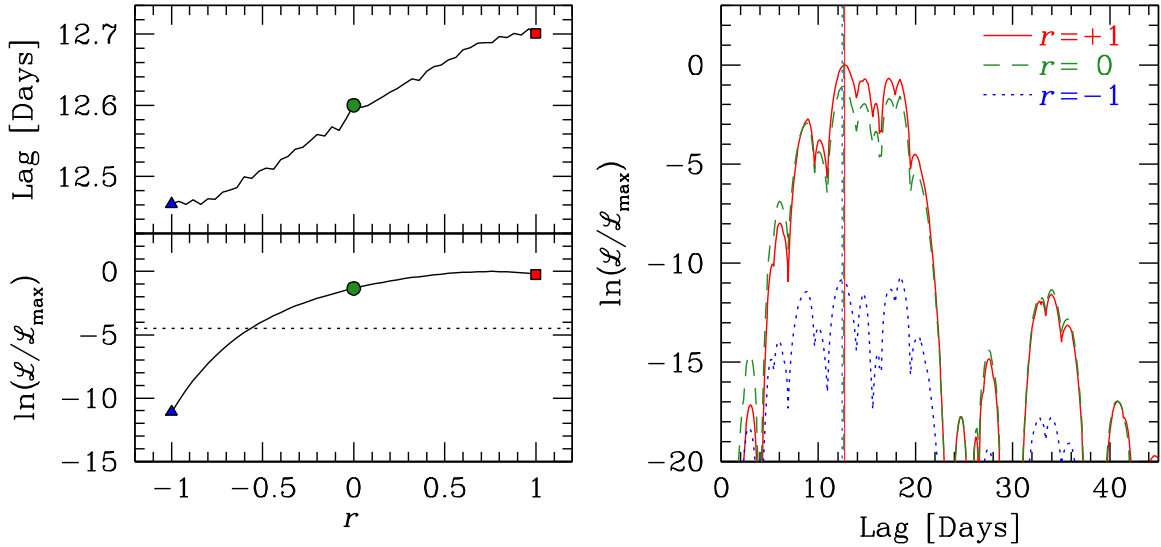
FIG. 5.— Sensitivity of the lag estimates to the noise correlation coefficient r between the Hβ and the continuum light curves of PG 0844. The left top panel shows the dependence of the lag on the correlation coefficient r. The left bottom panel shows the corresponding change in the likelihood function with r at the best-fit lag. In these panels, the blue triangle, green circle, and red square mark the results for $r = -1, 0, +1$, respectively, and the dotted line indicates the 3σ limit of the likelihood function. The right panel compares the lag likelihood distribution for these 3 cases: $r = -1$ (blue dotted curve), 0 (green dashed), and $+1$ (red solid), respectively. The dashed lines in the two right panels indicate the position of the best-fit lag, which is almost the same for all 3 cases.

data points, its width approaches that of the measurement errors and then grows as the distance Δt from any data point increases. The variance from the process initially increases as $\hat{\sigma}|\Delta t|^{1/2}$, but then saturates at the overall process variance once $|\Delta t| \gg \tau_d$. Thus, in the extrapolated regions we see the model light curve becomes a constant and the error snake expands and then becomes constant.

The three objects shown in Figure 2 represent three typical levels of light-curve sampling quality for the objects we consider. Generally, the light curves of the Palomar–Green (PG) quasars obtained by Kaspi et al. (2000) were sampled every 1–4 months over a baseline as long as 7.5 yr, as opposed to most of the low-luminosity Seyfert 1 AGNs that were more densely sampled over shorter baselines. The rest of the sample mainly consists of nearby bright Seyfert galaxies (Peterson et al. 1998) whose light curves are sparsely sampled over a short baseline. Peterson et al. (2004) discuss the data in detail. In addition, we also include new light curves from a recent high sampling rate, multi-month reverberation mapping campaign on six local Seyfert galaxies (Denney et al. 2010).

We expect the damping timescales τ_d to show correlations with the physical characteristics of the accretion disk such as the mass of the central black hole, and the AGN luminosity (Peterson 2008). Kelly et al. (2009) demonstrated this scaling relationship between τ_d and L_{AGN} by performing a linear regression of τ_d on L_{AGN}, while Collier & Peterson (2001) also found a positive correlation between the characteristic timescale and black hole masses. Their characteristic timescale, which is defined by the timescale where the structure functions flattened, is roughly equivalent to τ_d. Figure 3 shows that the more luminous central engines have longer exponential damping timescales, as we would expect from Kelly et al. (2009), up to any minor differ-

ences from fitting fluxes rather than magnitudes. Note that MacLeod et al. (2010) argue that the dependence of τ_d on black hole mass M_{BH} is the real driver of the correlation between τ_d and luminosity. We can use these correlations to estimate τ_d for sources lacking sufficiently good light curves.

4. ESTIMATING EMISSION-LINE LAGS

As our first application of the SPEAR method we recompute the lags of 101 emission-line light curves for 31 objects in the literature (the compilation of Peterson et al. 2004 with the addition of data from Bentz et al. 2006, Grier et al. 2008, and Denney et al. 2006, 2010). We carried out the analysis in three stages. First, as discussed in §3, we modeled the continuum alone to determine the range of process parameters $(\tau_d, \hat{\sigma})$ consistent with the continuum light curve. We use this distribution of estimated τ_d and $\hat{\sigma}$ as a prior for the joint models of the continuum and line light curves in order to avoid the secondary solutions with $\tau_d \to 0$ as discussed in §2. Second, for each joint model, we find the best-fit top hat transfer function (Equation 22) which maximizes the model likelihood calculated by Equation (17), along with an updated set of process parameters. Finally, we ran an MCMC analysis on each joint model to calculate the statistical confidence limits on each best-fit parameter found by global optimization on a grid, especially the time lag. We then compare these estimates to those derived from previous CCF analyses. We refer to these models as the "single-line" fits since they are solving for a single top-hat transfer function. The dotted histogram in Figure 1 shows the χ^2/dof distribution of the single-line model. It has a similar shape to the χ^2/dof distribution of the stochastic model for only the continuum light curve, and confirms that the statistical model provides a good fit to the quasar variability, as well as the overall *ansatz* that the Hβ variability is a scaled and smoothed
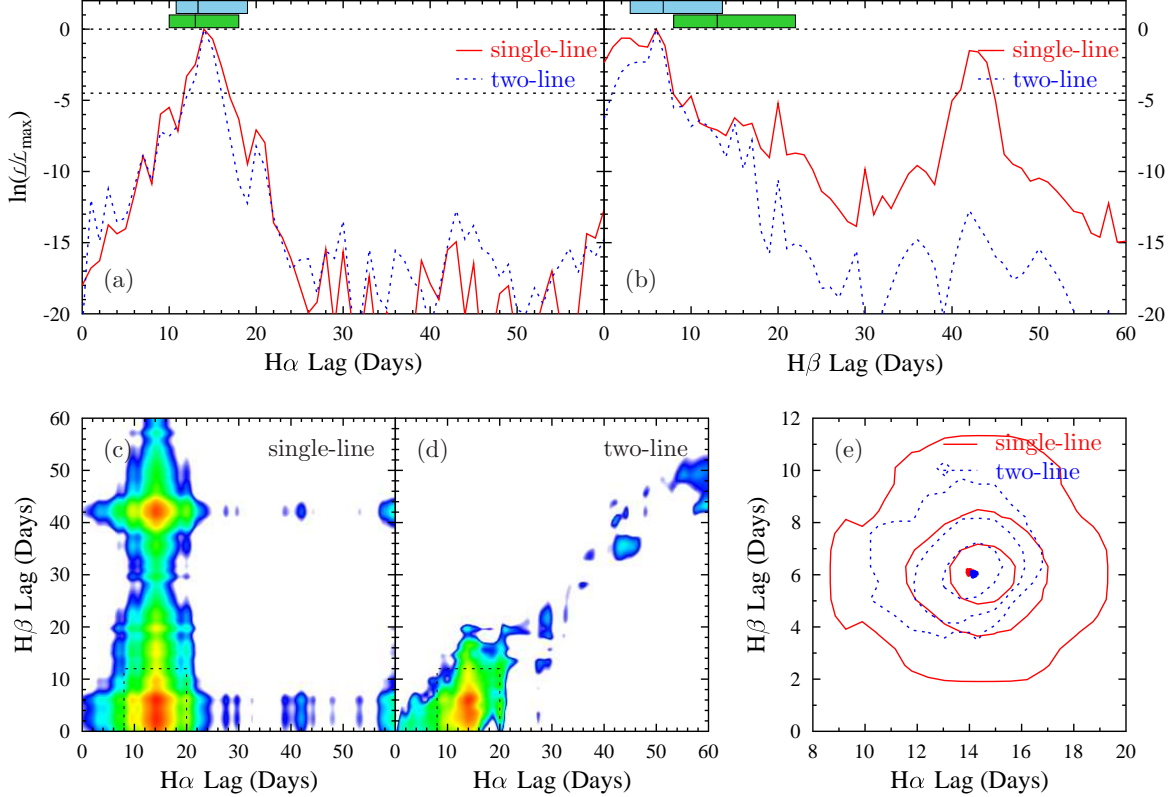
FIG. 6.— Comparison between independent (single-line) and joint (two-line) fits to the Hα and Hβ light curves of NGC 3516. The red solid lines are the estimate from the single-line fits, while the blue dashed lines are those from the two-line fits. The top left (right) panel compares the likelihood distributions of the two fits for the Hα (Hβ) line. The interval between the two dotted lines corresponds to a 3σ range in the likelihood, while the two blocks above indicate the $\pm 1\sigma$ range of the CCF peak analysis (upper) and CC centroid distribution (lower), where the central lines mark the τ_{peak} and τ_{cent} values, respectively. The two bottom left panels shows the color-coded covariance map between the two lags for the single-line and two-line fits, respectively. The contours in the bottom right panel compare the confidence levels calculated from MCMC for the Hα/Hβ lags near the peak (black boxes inside left two panels). Working outward, the three contour curves are for 1σ, 2σ and 3σ levels, respectively. Note that those are all observed-frame lags and the Hβ light curve here is the older of the two we have for NGC 3516.

version of the continuum. The χ^2/dof distribution of the single-line model is somewhat worse than for fitting the continuum alone, but still reasonably consistent with statistical expectations.

For the sake of uniformity of emission-line species in the comparison between the SPEAR and the CCF methods, and to avoid confusion in the figures for sources with multiple line observations, we will focus on the the 66 Hβ light curves in our subsequent analyses, and tabulate all the other emission-line lags we successfully computed with SPEAR in Table 1.

Figure 4 shows the comparison between CCF centroid time lags τ_{CCF} and our lags τ_{SPEAR} for all the Hβ lines. The range of uncertainties for τ_{CCF} contains 68.3% of Monte Carlo realizations in the cross-correlation centroid distribution (CCCD), while our estimated error boundaries are defined by the 68.3% ($\ln\mathcal{L}/\mathcal{L}_{\max} = 0.5$) confidence levels that encloses the best-fit lags (i.e., $\pm 1\sigma$ errors if the probability distribution is Gaussian in both cases). Based on the structure of the lag probability distribution, we can divide the "single-line" fits into five quality groups:

(I) In most of the cases (43 of 66), the likelihood distribution for the lags has a single peak and there is an unambiguous Hβ lag.

(II) In 9 cases, the likelihood distribution has multiple peaks with significant ($> 3\sigma$) likelihood differences. This occurred for one season of Akn 120 (JD49980–50175)[5], Mrk 110 (JD48953–49149), and Mrk 590 (JD49183–49338); two seasons of Mrk 79 (JD48193–48393 and JD49996–50220); NGC 4051, PG 0844[6], PG 1411, and PG 1617. Compared to our estimate, the CCF analysis picks a lower likelihood peak or aliases several peaks into one broad peak. Generally, the two peaks are so close that the differences between the results from the two methods are insignificant compared to the uncertainties.

(III) In 7 cases, the likelihood distribution has multiple peaks of comparable significance ($\leq 3\sigma$: one series of NGC 3516 (JD47894–48047), Fairall 9, PG 0026, PG 0052, PG 1211, PG 1226, and PG 1307). They are shown in Figure 4 as the objects with a dashed line connecting the possible solutions. The traditional CCF method seems to find one broad peak for these sources, rather than multiple peaks, leading to large reported uncertainties for the estimate of τ_{CCF}. These degeneracies are largely caused

---

[5] For brevity, we retain only the five least significant digits of the Julian Date.

[6] For brevity, we truncate the PG coordinate identifiers to right ascension only since this introduces no ambiguity in the present small sample.
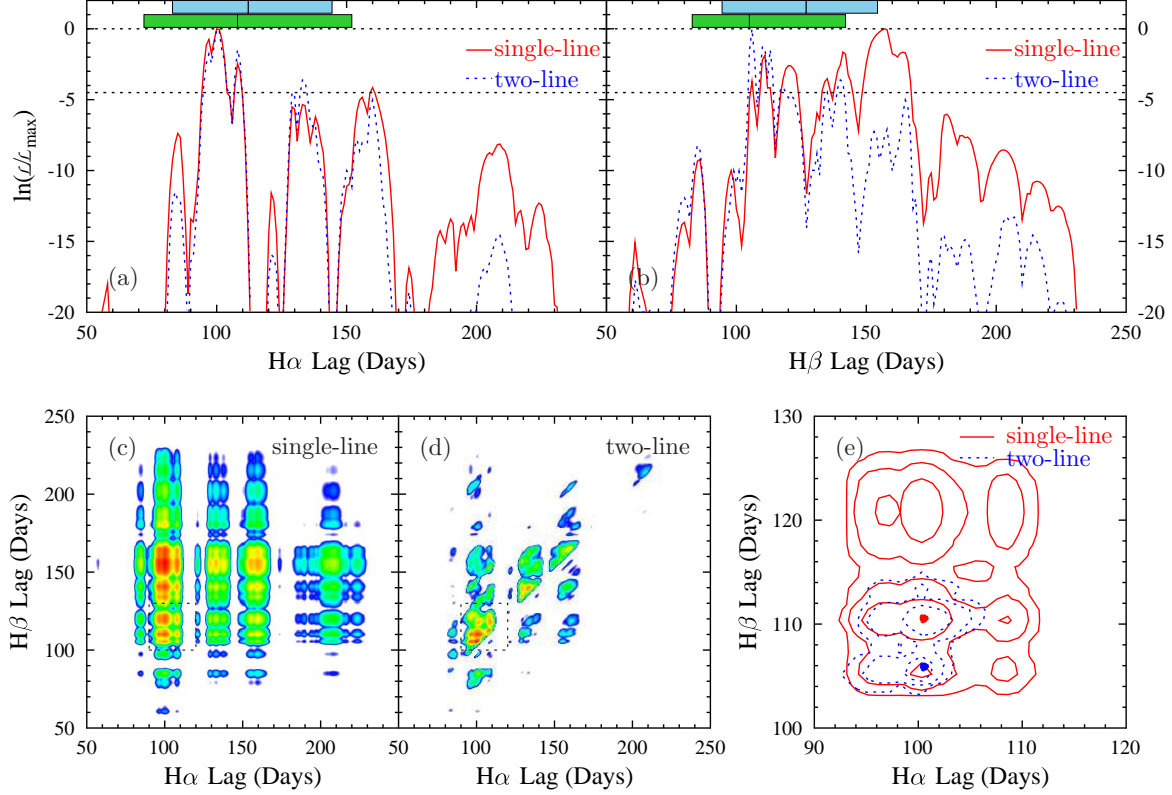
Fig. 7.— Comparison between independent (single-line) and joint (two-line) fits to the Hα and Hβ light curves of PG 0026. The format is the same as in Figure 6.

by poor light curve sampling that allows the light curve of the emission line to be mapped into the sampling gaps of the continuum. This problem is worst for the PG objects, which have many "seasonal gaps" over the long observing baselines ($\sim$ 7.5 yr), leading to a clustering of solutions around 180 days in the observed-frame. Such seasonal aliasing problems affect the CCF-based methods as well (Grier et al. 2008).

(IV) In four cases, the light curves are very poorly sampled: IC 4329A, one season on NGC 4593 (JD47894–48049), one season of Mrk 279 (JD47205–47360), and one season of NGC 3227 (JD47894–48045). These cases were also flagged as unreliable by Peterson et al. (2004), so we exclude them from our subsequent analyses.

(V) The lags derived from the SPEAR method appear to be wrong in two cases, 3C 120 and PG 1613. We also exclude both from our subsequent analyses. The 3C 120 light curves have a baseline of 7 years, but are very sparsely sampled. The CCF method finds a lag $\sim$ 40 days in the observed frame. Although we find a sub-peak at 40 days, the model favors another peak of much higher significance at 259 days. For PG 1613 we obtain a lag of $\sim$ 575 days in the observed-frame, much larger than the $\sim$ 50 day CCF estimate. In both cases, the longer lag is favored because it minimizes the data overlap — 259 and 575 days put most of the line data in the seasonal gaps, and many points also lie before the start of the continuum light curve. This

is essentially an aliasing problem in our method. We also note that the continuum flux varied by up to 50% over the 7 year span of the light curves. We know empirically that the scaling coefficient A in the transfer function is inversely correlated with ionizing continuum flux (see the right panel of Figure 10 and the discussion in §8), but we treat A as a constant parameter in each individual fit. This may create problems for light curves with the significant long term trends observed for these objects. Allowing A to vary and adopting a prior that penalizes large lags that minimize light curve overlap would likely solve these problems.

5. MODEL TEST FOR CORRELATED ERRORS

Correlated errors have long been viewed as a problem in traditional CCF analysis. Observations made at a common epoch are inevitably correlated by the processes required for calibration, light curve extraction, broad/narrow line modeling and removal of host or FeII contamination. Because no assumption about the properties of the noise matrix N was made in §2, it is easy to include the effects of correlated errors within our approach. While we did not make an extensive survey of our ability to model noise correlations between the continuum and lines, we did carry out some experiments for objects noted as potentially having strong covariances by Peterson et al. (2004).

The simplest test is to introduce a covariance factor $-1 \le r \le 1$ and add off-diagonal terms to the noise matrix N for line and continuum points measured at the same epoch of $N_{cl}(t,t) = N_{lc}(t,t) = r\sigma_l(t)\sigma_c(t)$ in order to examine the sensitivity of the lag estimates to corre-

lated noise between the line and the continuum measured at each epoch. This should be present in the data at some level because of the challenge of consistently subtracting the contribution of the host galaxy to the line and the continuum in the presence of variable observational conditions.

Figure 5 illustrates the effects of adding off-diagonal correlated noise terms on the Hβ lag estimate of PG 0844. The shift in the estimated lag (left top panel) induced by r varying from -1 to $+1$ is only about 0.25 days, much smaller than the median sampling interval of the light curves. The corresponding change in the likelihood (left bottom panel) shows a plateau at $r > 0$ and slowly asymptotes to a maximum at $r = +1$, suggesting that the errors in the two light curves are positively correlated. The lag likelihood distribution (right panel) changes if we assume different levels of correlations r between the light curves. While the overall lag likelihood is greatly depressed in the $r = -1$ case, the likelihood distributions are nearly identical in the $r = 0$ and $r = +1$ cases. However, the peaks near the best lag estimate (~ 12 days) are slightly more significant in the $r = +1$ case than in the $r = 0$ case. We explored this issue for several other systems, and generally the impact on the estimated lag is negligible, although different levels of (anti-)correlations are detected.

6. JOINT ANALYSIS OF MULTIPLE LINES

In §4, we found that poor light curve sampling was a significant problem in many systems, particularly in objects with observed-frame lags on time scales similar to the seasonal gap spacing. However, if multiple lines have been measured, then we have significant, additional data to better sample the light curves under our overall *ansatz* that all light curves are scaled, smoothed, and displaced versions of the continuum. Simultaneous fits also determine the covariance between the lags of the different lines. In this section, we explore simultaneously fitting the continuum and two emission-line light curves (hereafter "two-line" fits, as opposed to the "single-line" fits in §4, as we are now fitting two top-hat transfer functions).

Figure 6 summarizes the significant improvement in estimating the Hβ time lag of NGC 3516 of the Wanders et al. (1993) data (JD47894–48047) after including the Hα light curve (two-line) compared to using the Hβ line alone (single-line). NGC 3516 is a case where the single-line Hβ fits shows a secondary peak at ~ 42 days whose likelihood relative to the main peak at ~ 6 days is high, $\ln(\mathcal{L}_{2nd}/\mathcal{L}_{max}) = -1.5$ (solid curve in panel b). The Hα fit does not show such a secondary peak (panel a). When we fit both simultaneously, the Hα light curve together with its well-determined lag adds extra information to the continuum light curve, and thus better constrains the Hβ lag. The second Hβ peak is suppressed and there is a single unambiguous Hβ lag for the two-line fit (dotted curve in panel b). The improvement is most clearly seen in the structure of the Hα/Hβ lag likelihood plane (panel c and d). If we zoom in on the remaining peak and run a MCMC chain using a flat prior on lags in the zoomed region, we can see that the two-line fits not only suppress the secondary peaks but also shrink the uncertainties in the primary peak to produce better results for both lines (panel e).

The joint analysis of multiple lines is especially useful for the PG objects, whose light curves show observational gaps of period ~ 180 days in the observed-frame. In the single line fits, the model would always show (sub)peaks for lags ~ 180 days because of the seasonal aliases (the seasonal stripes in Figure 4). It is not possible, however, to do this for 2 lines simultaneously, so the two-line fits largely eliminate seasonal aliasing. Figure 7 illustrates this for PG 0026. In particular, the broad Hβ likelihood distribution shrinks significantly and the maximum likelihood lag drops from ~ 160 days to ~ 106 days (~ 140 to ~ 93 in the rest frame) and is in better agreement with the Hα results. Although the traditional CCF method makes similar estimates (green and blue bands in two top panels), it yields significantly larger uncertainties by aliasing several peaks into one broad CCF centroid distribution.

We performed similar joint analyses for the 21 sources for which we have multiple emission line light curves and recompile the results for the Hβ lags, as shown in Figure 8. Fortunately, all the sources whose Hβ lags were found to be ambiguous in the single-line fits (i.e., the 7 Hβ lags from groups III in §4) are improved by the two-line fits, although the degree of improvement varies. We also dropped lag estimates that were either flagged as unreliable or believed to be wrong (i.e., the 6 Hβ lags from groups IV and V in §4) and keep only those objects deemed to give robust estimates of lag by our method (i.e., the 60 Hβ lags from groups I, II and III). To illustrate the quality of the final result for each source, we divide all 60 remaining sources into 4 new groups based on the results of both the single-line fits in § 4 and the two-line fits, using different symbols for the 4 new groups in Figure 8.

(A) The 43 group I light curves from § 4 with a single unambiguous Hβ lag. Seven of the objects have light curves of lines other than Hβ to carry out two-line fits, but they provided little gain when the single-line fits already provided good lag estimates.

(B) The 10 group II sources from § 4 with a robust Hβ lag estimate but potentially larger uncertainties due to the presence of low significance ($> 3\sigma$) subpeaks in the lag likelihood distribution. Most of those sources do not have the multiple line light curves needed to carry out two-line fits.

(C) The four group III sources (NGC 3516, PG 0026, PG 0052, and PG 1307) from §4 with multiple peaks in the single-line lag likelihood distribution where the ambiguity is removed by the two-line fits.

(D) The three group III sources (Fairall 9, PG 1211, and PG 1226) from §4 with multiple peaks in the single-line lag likelihood distribution where the two-line fits fail to remove the ambiguity. We picked the most significant peak as the solution and extended the uncertainty to cover all the possible solutions.

Recall that we have dropped the 6 group IV and V sources (IC 4329A, NGC 4593, one season of Mrk 279, one season of NGC 3227, 3C 120, and PG 1613) out of all 66 Hβ light curves following the discussion in §4. Green circles, blue pentagons, dark violet squares, and
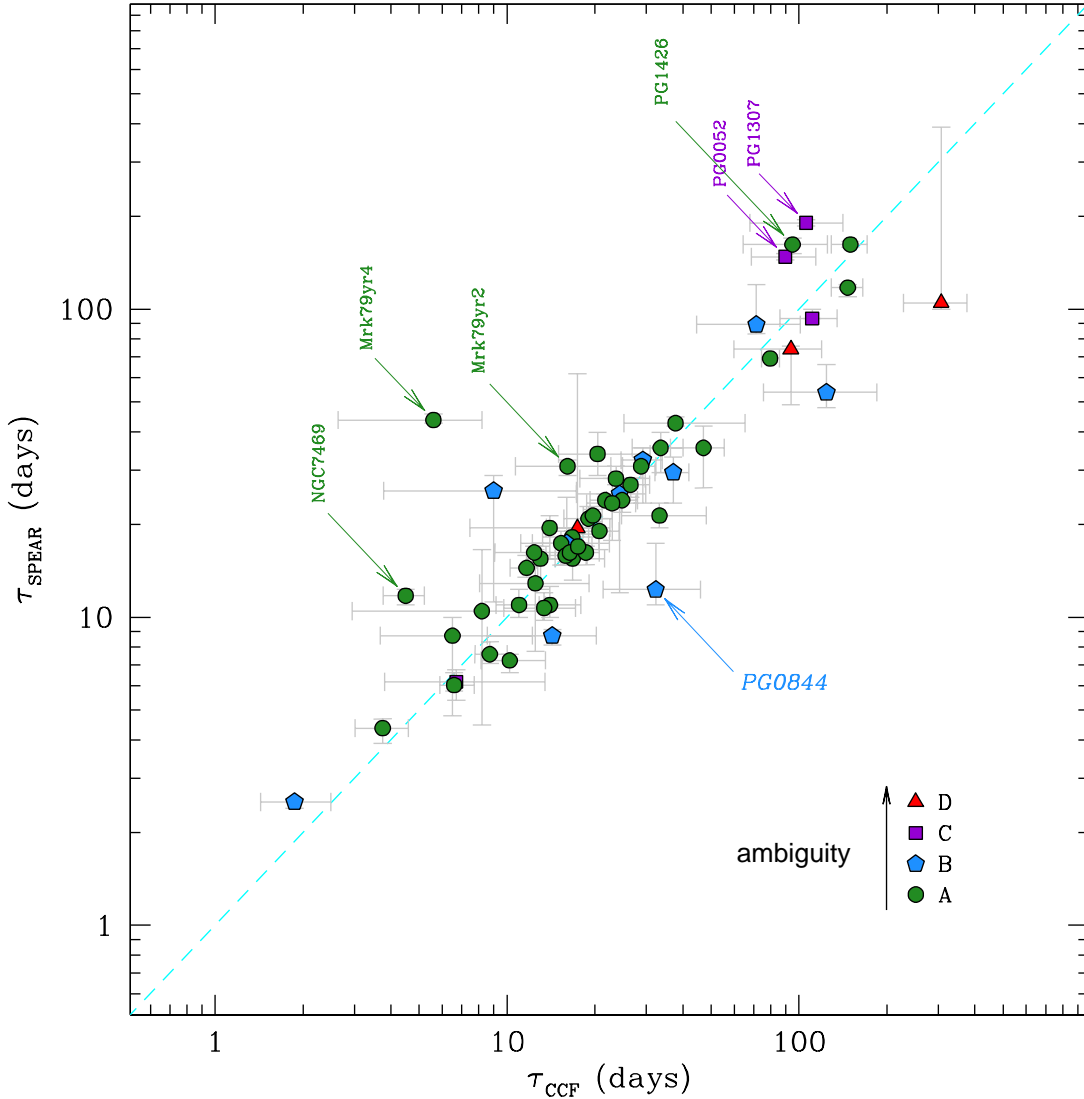
FIG. 8.— Comparison of the Hβ time lags from CCF analysis and the SPEAR method, similar to Figure 4, updated where we have used the two-line fits and dropping the 6 unreliable sources. Four types of symbols are used to indicate our estimate for increasing levels of ambiguity in the lag estimate. Objects with inconsistent lag estimates between the two methods are labeled.

red triangles correspond to sources of group A, B, C, and D, respectively. There is general agreement between the two methods, but also several discrepancies, as 7 of our Hβ lag estimates are inconsistent with the CCF results given their error estimates. We marked these sources in Figure 8 and now discuss each case individually,

NGC 7469. — We estimate an Hβ lag of $11.7^{+0.5}_{-0.7}$ days, as opposed to $\tau_{\rm CCF} = 4.7^{+0.7}_{-0.8}$. However, if we use a Dirac delta function for the transfer function instead of a tophat, the estimated time lag changes to 4.3 days, in agreement with the CCF result. Thus, the discrepancy originates from the improvement of fit with a tophat smoothing kernel. The continuum of NGC 7469 was intensively monitored to search for time lags between the UV and optical continuum (Collier et al. 1998), so its continuum light curve is densely sampled while the Hβ light curve is much less so. The model has to smooth the continuum light curve heavily (i.e., a broad tophat

width) to obtain a good fit, which at the same time shifts the time lag estimate to a longer value than it would be with a zero width (i.e., a delta function). This is suggestive of the continuum errors being underestimated, or a more realistic transfer function is required.

Mrk 79 (years 2 and 4). — In both cases, we estimate larger time lags than the CCF results, although there are sub-peaks which correspond to the CCF lags. For year 2 (JD47838–48044), while the CCF centroid gives a lag of $16.4^{+6.7}_{-6.7}$ days, the CCF peak estimate is 19^{+11}_{-12} days, more consistent with our estimate of $30.9^{+1.4}_{-2.1}$ days. For year 4 (JD49996–50220), Peterson et al. (2004) flagged it as "unreliable" for the poor light curve sampling. Our method shows a dense array of sub-peaks in the lag likelihood distribution, but the most significant peak is at $43.6^{+1.7}_{-0.8}$ days.
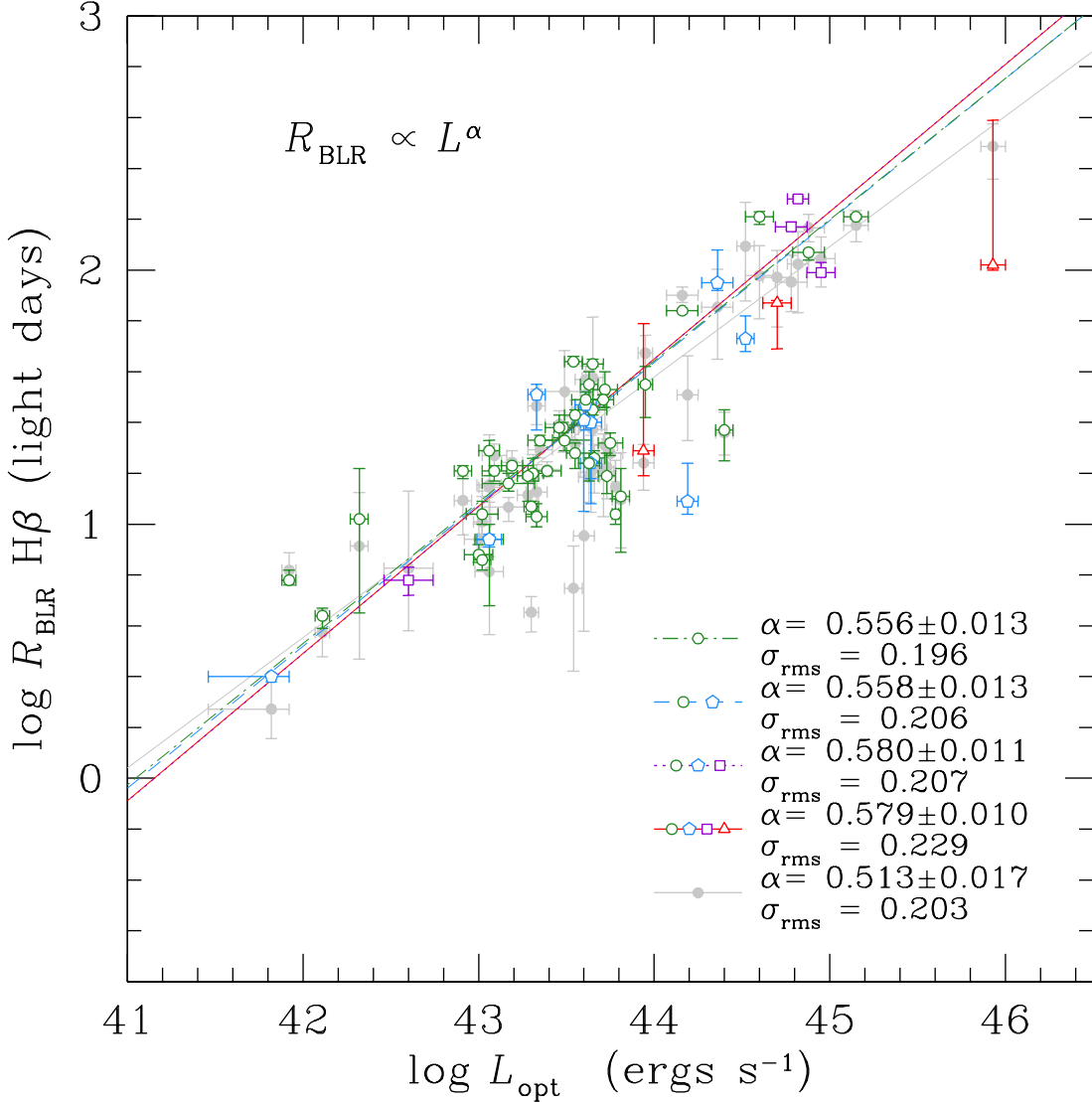
$$R_{\rm BLR} \propto L^{\alpha}$$

$\alpha = 0.556 \pm 0.013$
$\sigma_{\rm rms} = 0.196$
$\alpha = 0.558 \pm 0.013$
$\sigma_{\rm rms} = 0.206$
$\alpha = 0.580 \pm 0.011$
$\sigma_{\rm rms} = 0.207$
$\alpha = 0.579 \pm 0.010$
$\sigma_{\rm rms} = 0.229$
$\alpha = 0.513 \pm 0.017$
$\sigma_{\rm rms} = 0.203$

FIG. 9.— The $R_{\rm BLR}-L$ relation for Hβ. The luminosity is $\lambda L_{\lambda}(5100\,\text{Å})$ and the BLR radius is equivalent to the lag in units of light days. The open symbols and gray solid circles indicate the measurement from SPEAR method and from CCF method for the same set of sources, respectively. The gray solid curve is the fit to the CCF $R_{\rm BLR}-L$ relation, while the rest of the curves are the fits to the SPEAR $R_{\rm BLR}-L$ relation, using four subsets of the sources (see Table 2 for details of each fit). The slope of the fit to the SPEAR $R_{\rm BLR}-L$ relation α is steeper than the CCF relation, but the two are consistent within the uncertainties. $\sigma_{\rm rms}$ is the rms scatter of each fit.

PG 0844. — As discussed in § 5, the CCF estimate of the Hβ lag ($34.4^{+14.6}_{-14.2}$) for PG 0844 is likely susceptible to correlated errors, while our method estimates a lag of $12.2^{+5.2}_{-1.3}$ days regardless of the value of correlation coefficient r.

PG 0052. — We estimate an Hβ lag of $149.3^{+4.2}_{-1.8}$ days, as opposed to $\tau_{\rm CCF} = 103^{+28.3}_{-27.8}$. The single-line fit shows multiple peaks and usually one would be inclined to mistrust a peak at the seasonal alias (a rest-frame lag of 150 days corresponds to 170 days in the observed-frame). However, the joint Hα/Hβ fit clearly reinforced this solution.

PG 1307. — We estimate an Hβ lag of $188.8^{+5.7}_{-3.7}$ days, as opposed to $\tau_{\rm CCF} = 121.9^{+41.6}_{-53.8}$. The joint H$\alpha$/H$\beta$ fit suppressed the false peak which corresponds to the $\tau_{\rm CCF}$

lag, favoring a longer lag that is more consistent with lags of the other Balmer lines.

PG 1426. — We estimate an Hβ lag of $161.6^{+6.9}_{-11.1}$ days, as opposed to $\tau_{\rm CCF} = 103.2^{+32.5}_{-40.3}$. Similar to PG 0052 and PG 1307, the joint Hα/Hβ fit reinforced a solution which is otherwise susceptible to the seasonal gap effect.

We carried out a similar analysis for each data set, including all emission lines besides Hβ, as summarized in Table 1. Note that in the table we only include 87 light curves for which we have successfully computed lags. The object is identified in column (1). The emission line and its light curve Heliocentric Julian Date range are listed in columns (2) and (3), respectively. Column (4) gives the rest-frame time lag estimate from the SPEAR method, while column (5) indicates the associated "ambiguity" (i.e., the group membership) defined above.
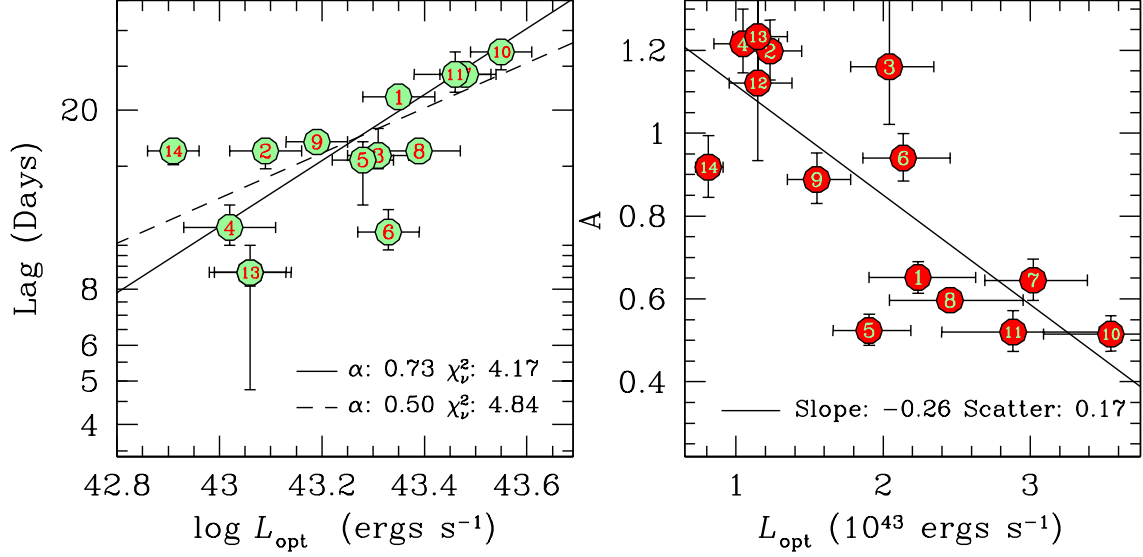
FIG. 10.— Lag (left) and scaling coefficient (right) of the Hβ transfer function as a function of continuum luminosity from 14 years of NGC 5548 data. The best-fit slopes are also reported for each panel and shown by the black solid lines. The black dashed line in the left panel is the best fit with a fixed slope of 0.50. The number inside each solid circle indicates the year of observation for each light curve starting from Dec. 1988. Note that in the left panel the point for year 12 is hidden under that of year 13.

7. THE $R_{\rm BLR}$–L RELATION FOR Hβ

With the revised set of Hβ lags, and the starlight-corrected optical luminosity of each AGN from Bentz et al. (2009), we have calculated the fit to the $R_{\rm BLR}$–L relationship for our sample

$$R_{\rm BLR} = C \cdot \left(\frac{L}{10^{43.5}\,\mathrm{ergs\,s^{-1}}} \right)^{\alpha} \quad (23)$$

and compared it to that based on CCF lags in Figure 9. We obtained a slope $\alpha = 0.579 \pm 0.010$ for all the SPEAR lags regardless of the level of "ambiguity" at which we probe the slope. This slope is slightly steeper than previous estimates, and only marginally consistent with the naïve theoretical prediction of $\alpha = 0.5$. Compared to the CCF-based $R_{\rm BLR}$–L fit of the same sample of AGNs (blue filled circles), our $R_{\rm BLR}$–L fit has a steeper slope but comparable rms scatter $\sigma_{\rm rms}$, which grows smaller as we use more reliable lags. Table 2 gives the results from the different fits using the 4 combinations of groups indicated by column (1). Column (2) gives the number of data points used in each fit. We fit each combinatorial data set using lag estimates from both the SPEAR (columns 3–6) and CCF methods (columns 7–10). Two parameters in Equation (23) are listed in columns (3) and (4) for SPEAR method, and in column (7) and (8) for CCF method, respectively. Column (5) and (6) give the χ^2/dof and rms scatter for our fit, while column (9) and (10) give these statistics correspondingly for the CCF method.

Our $R_{\rm BLR}$–L fits have a larger χ^2/dof than the CCF ones. This does not necessarily mean they are poorer fits, because our lag estimates generally have tighter error-bars than the CCF estimates. It could indicate that our approach underestimates uncertainties, that the CCF method overestimates uncertainties, or that we are not taking into account intrinsic scatter in the $R_{\rm BLR}$–L relationship. Since most of the group C and D sources

are high-redshift luminous PG objects, the rms scatter for our method decreases from 0.229 dex to 0.196 dex after dropping them from the fit. Three outliers from the CCF $R_{\rm BLR}$–L relation (NGC 7469, years 1 and 4 of Mrk 79) are also the sources where our lag estimates are inconsistent with CCF results. When we use our lag estimates, these three CCF outliers lie on the $R_{\rm BLR}$–L relation, which reduces the rms scatter near $L_{\rm opt} \sim 10^{43.5}$ ergs s^{-1}. Note that there is significant scatter in the $R_{\rm BLR}$–L relation even for multiple estimates for a single source, as shown in the left panel of Figure 10 for NGC 5548.

8. $R_{\rm BLR}$–L RELATION OF NGC 5548 REVISITED

So far, we have carried out our calculations assuming that the parameters are constant during a season. This is likely true for the underlying variability process. If we model either the full continuum light curve or the individual seasons, we find estimates for the process parameters $\tau_{\rm d}$ and $\hat{\sigma}$ that are statistically consistent. We do observe lags that vary from season to season, and these are arguably correlated with luminosity. If so, they should also be varying within seasons, and we have not accounted for this. Similarly, we assume the scaling between the continuum and line fluxes does not vary over a season, although we do observe it to vary between seasons.

The nearby Seyfert 1 galaxy NGC 5548, with its many continuous years of monitoring data, serves as an ideal example of an AGN changing its variability levels from season to season. Figure 10 illustrates the continuum flux dependence of both the Hβ lag $\langle \tau \rangle$ and the scaling coefficient A for 14 seasons of NGC 5548 data. We clearly see trends that the lag increases with luminosity and the amplitude of the response diminishes. If we fit the lag, we find a steep slope, $\langle \tau \rangle \propto L^{0.73 \pm 0.10}$ that is inconsistent with the expected $\langle \tau \rangle \propto L^{0.5}$. However, the poor fit ($\chi^2/dof = 4.17$) suggests that either the uncertainties are underestimated or intrinsic scatter dominates

TABLE 1
Rest-Frame Lag Estimates

Object (1)	Line (2)	Julian Dates (−2400000) (3)	$\tau_{\rm SPEAR}$ (days) (4)	Group (5)
3C 390.3	Hβ	49718–50012	$27.9^{+2.4}_{-1.5}$	A
3C 390.3	Lyα	49718–50147	$11.9^{+34.5}_{-4.6}$	D
3C 390.3	C IV λ1549	49718–50147	$15.0^{+2.0}_{-3.0}$	C
Akn 120	Hβ	48148–48344	$35.7^{+6.7}_{-9.2}$	A
Akn 120	Hβ	49980–50175	$29.7^{+3.3}_{-5.9}$	B
Fairall 9	Hβ	50473–50665	$19.4^{+42.1}_{-3.8}$	D
Fairall 9	He II λ1640	50473–50713	$12.0^{+0.9}_{-3.9}$	C
Fairall 9	Lyα	50473–50713	$12.1^{+0.5}_{-0.5}$	C
Mrk 79	Hβ	47838–48044	$25.5^{+2.9}_{-14.4}$	B
Mrk 79	Hβ	48193–48393	$30.9^{+1.4}_{-2.1}$	A
Mrk 79	Hβ	48905–49135	$17.2^{+7.3}_{-2.2}$	B
Mrk 79	Hβ	49996–50220	$43.6^{+1.7}_{-0.8}$	A
Mrk 110	Hβ	48953–49149	$25.3^{+2.3}_{-13.1}$	B
Mrk 110	Hβ	49751–49874	$33.9^{+6.1}_{-5.3}$	A
Mrk 110	Hβ	50010–50262	$21.5^{+2.2}_{-2.1}$	A
Mrk 279	Hβ	50095–50289	$18.3^{+1.2}_{-1.1}$	A
Mrk 290	Hβ	54184–54301	$7.7^{+0.7}_{-0.5}$	A
Mrk 335	Hβ	49156–49338	$15.3^{+3.6}_{-2.2}$	A
Mrk 335	Hβ	49889–50118	$12.9^{+3.6}_{-5.0}$	A
Mrk 509	Hβ	47653–50374	$69.9^{+0.3}_{-0.3}$	A
Mrk 509	He II λ4686	47653–50374	$52.2^{+0.1}_{-0.1}$	D
Mrk 590	Hβ	48090–48323	$19.0^{+1.8}_{-2.6}$	A
Mrk 590	Hβ	48848–49048	$19.5^{+2.0}_{-4.0}$	A
Mrk 590	Hβ	49183–49338	$32.6^{+3.5}_{-8.8}$	B
Mrk 590	Hβ	49958–50122	$30.9^{+2.5}_{-2.4}$	A
Mrk 817	Hβ	49000–49212	$20.9^{+2.3}_{-2.3}$	A
Mrk 817	Hβ	49404–49528	$17.2^{+1.9}_{-2.7}$	A
Mrk 817	Hβ	49752–49924	$35.9^{+4.8}_{-5.8}$	A
Mrk 817	Hβ	54200–54330	$10.8^{+1.5}_{-1.0}$	A
NGC 3227	Hβ	48623–48776	$10.6^{+6.1}_{-6.1}$	A
NGC 3227	Hβ	54180–54273	$4.4^{+0.3}_{-0.5}$	A
NGC 3516	Hα	47894–48047	$14.0^{+0.7}_{-0.7}$	A
NGC 3516	Hβ	47894–48047	$6.1^{+0.5}_{-0.7}$	C
NGC 3516	Hβ	54181–54300	$14.6^{+1.4}_{-1.4}$	A
NGC 3783	Hβ	48607–48833	$7.3^{+0.3}_{-0.7}$	A
NGC 4051	Hβ	54180–54311	$2.5^{+0.1}_{-0.1}$	B
NGC 4151	Hβ	53430–53471	$6.0^{+0.6}_{-0.2}$	A
NGC 4593	Hβ	53430–53471	$4.5^{+0.7}_{-0.6}$	A
NGC 7469	Hβ	50237–50295	$11.7^{+0.5}_{-0.7}$	A
NGC 7469	Si IV λ1400	50245–50293	$2.0^{+0.4}_{-0.5}$	A
NGC 7469	C IV λ1549	50245–50293	$10.6^{+0.2}_{-0.2}$	A
NGC 7469	He II λ1640	50245–50293	$0.8^{+0.2}_{-0.2}$	A
PG 0026+129	Hα	48836–51084	$88.0^{+1.5}_{-3.5}$	B
PG 0026+129	Hβ	48545–51084	$92.7^{+7.0}_{-0.6}$	C
PG 0052+251	Hα	48837–51084	$157.6^{+2.3}_{-2.8}$	A
PG 0052+251	Hβ	48461–51084	$149.3^{+4.2}_{-1.8}$	C
PG 0052+251	Hγ	48461–51084	$154.9^{+1.9}_{-1.9}$	C
PG 0804+761	Hα	48319–51085	$133.4^{+8.6}_{-4.3}$	C
PG 0804+761	Hβ	48319–51085	$116.8^{+2.6}_{-7.3}$	A
PG 0804+761	Hγ	48319–51085	$71.1^{+46.5}_{-3.1}$	D
PG 0844+349	Hα	48319–51085	$20.8^{+0.4}_{-1.4}$	A
PG 0844+349	Hβ	48319–51085	$12.2^{+5.2}_{-1.3}$	B
PG 0844+349	Hγ	48319–51085	$17.7^{+2.5}_{-2.1}$	C
PG 0953+414	Hβ	48319–50997	$162.2^{+3.5}_{-2.9}$	A
PG 0953+414	Hγ	48319–50997	$160.2^{+3.3}_{-56.8}$	D
PG 1211+143	Hα	48319–51000	$76.3^{+0.7}_{-0.5}$	C
PG 1211+143	Hβ	48319–51000	$73.3^{+0.9}_{-25.4}$	D
PG 1211+143	Hγ	48319–51000	$57.7^{+15.8}_{-10.1}$	D
PG 1226+023	Hα	48361–50997	$380.0^{+40.7}_{-6.0}$	B
PG 1226+023	Hβ	48361–50997	$105.5^{+284.1}_{-5.2}$	D
PG 1226+023	Hγ	48361–50997	$263.8^{+9.0}_{-10.6}$	A
PG 1229+204	Hα	48319–50997	$45.7^{+2.8}_{-1.1}$	A
PG 1229+204	Hβ	48319–50997	$42.8^{+2.3}_{-1.1}$	A

TABLE 1
— Continued

Object (1)	Line (2)	Julian Dates (−2400000) (3)	$\tau_{\rm SPEAR}$ (days) (4)	Group (5)
PG 1307+085	Hα	49130–51000	$189.1^{+4.6}_{-3.6}$	A
PG 1307+085	Hβ	48319–51042	$188.8^{+5.7}_{-3.7}$	C
PG 1307+085	Hγ	48319–51042	$218.9^{+7.2}_{-124.8}$	D
PG 1411+442	Hα	48319–51038	$59.3^{+10.1}_{-6.7}$	A
PG 1411+442	Hβ	48319–51038	$53.5^{+13.1}_{-5.3}$	B
PG 1426+015	Hβ	48334–51042	$161.6^{+6.9}_{-11.1}$	A
PG 1617+175	Hα	48362–51085	$106.9^{+9.8}_{-13.3}$	B
PG 1617+175	Hβ	48362–51085	$88.2^{+31.0}_{-5.9}$	B
PG 2130+099	Hβ	54352–54450	$23.2^{+4.4}_{-5.8}$	A
PG 2130+099	He II λ4686	54352–54450	$32.0^{+3.9}_{-4.5}$	A
NGC 5548	Hβ	47509–47809	$21.2^{+0.8}_{-1.0}$	A
NGC 5548	Hβ	47861–48179	$16.3^{+0.8}_{-1.3}$	A
NGC 5548	Hβ	48225–48534	$15.8^{+2.1}_{-3.1}$	A
NGC 5548	Hβ	48623–48898	$11.0^{+1.2}_{-1.0}$	A
NGC 5548	Hβ	48954–49255	$15.3^{+1.4}_{-3.0}$	A
NGC 5548	Hβ	49309–49636	$10.8^{+1.4}_{-1.0}$	A
NGC 5548	Hβ	49679–50008	$24.2^{+1.3}_{-0.9}$	A
NGC 5548	Hβ	50044–50373	$16.1^{+0.3}_{-0.6}$	A
NGC 5548	Hβ	50434–50729	$16.8^{+0.4}_{-0.2}$	A
NGC 5548	Hβ	50775–51085	$26.9^{+1.5}_{-2.2}$	A
NGC 5548	Hβ	51142–51456	$23.8^{+3.1}_{-2.3}$	A
NGC 5548	Hβ	51517–51791	$8.8^{+1.3}_{-3.9}$	A
NGC 5548	Hβ	51878–52174	$8.7^{+0.5}_{-0.5}$	B
NGC 5548	Hβ	54180–54332	$16.3^{+1.0}_{-1.2}$	A

NOTE. — Lag estimates and confidence limits for Groups A and B are calculated by the single-line fits, while those for Groups C and D are from the two-line fits.

the goodness-of-fit. If we rescale the uncertainties so that the best-fit model has $\chi^2/dof \equiv 1$, the flatter $L^{0.5}$ slope is not ruled out, with a $\Delta\chi^2$ of only 0.16.

These problems can be addressed by making the lags and the line-to-continuum scaling a function of the continuum luminosity. For the luminosity dependence of lags, the simplest approach would be to de-lag the line light curve as $\langle\tau\rangle \propto L^\alpha$ instead of shifting the entire light curve by the same t_{lag}, and then optimize the fits over the additional parameter α. Unfortunately, we cannot fit the full NGC 5548 light curve because the resulting matrix dimensions are impractically high (K=3085 data points). We instead estimate the normalized likelihood distribution for α in each season and then combined the likelihoods, as shown in Figure 11 (we did not include year 13, which was part of the less reliable group B). This "breathing" effect is clearly detected, and the logarithmic slope estimate of $\alpha = 0.44^{+0.20}_{-0.08}$ is consistent with the naïve expectation $\alpha = 1/2$ and the $R_{\rm BLR}$–L relation in Figure 9. Using almost the same set of light curves from NGC 5548 (we add year 14 and exclude year 13), Cackett & Horne (2006) find a much shallower slope (0.1–0.46) with a luminosity-dependent delay map, in better agreement with the prediction of photoionization models ($\sim$ 0.23; Korista & Goad 2004). However, their small correction for the host galaxy starlight may artificially flatten their estimate of the slope (Bentz et al. 2007). Note that for this experiment we did not make the line-to-continuum scaling coefficient A a function of continuum luminosity in the fit. Such a full scale calculation should be carried out using the complete data set.

TABLE 2
BLR Size-Luminosity Relation

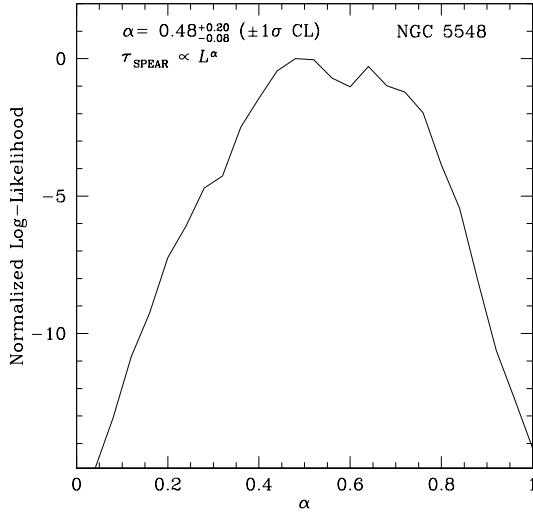| Groups Included (1)	N (2)	C_{SPEAR} (lt-days) (3)	α_{SPEAR} (4)	χ^2_{SPEAR} (5)	$\sigma^{\mathrm{SPEAR}}_{\mathrm{rms}}$ (dex) (6)	C_{CCF} (lt-days) (7)	α_{CCF} (8)	χ^2_{CCF} (9)	$\sigma^{\mathrm{CCF}}_{\mathrm{rms}}$ (dex) (10)
A,B,C,D	60	1.36 ± 0.01	0.579 ± 0.010	8.13	0.229	1.32 ± 0.01	0.513 ± 0.017	3.50	0.203
A,B,C	57	1.36 ± 0.01	0.580 ± 0.011	8.52	0.207	1.33 ± 0.01	0.519 ± 0.019	3.54	0.205
A,B	53	1.36 ± 0.01	0.558 ± 0.013	8.39	0.206	1.33 ± 0.01	0.521 ± 0.020	3.81	0.213
A	43	1.36 ± 0.01	0.556 ± 0.013	9.44	0.196	1.32 ± 0.01	0.518 ± 0.020	4.22	0.211

FIG. 11.— Likelihood distribution of α for 13 years of NGC 5548 light curves. The normalized log-likelihood is calculated by adding the likelihood distribution functions for the 13 individual years together.

9. DISCUSSION

We have demonstrated that direct fitting of continuum and line light curves is a viable approach to measuring reverberation lags, confirming the initial study of Rybicki & Kleyna (1994). It provides a full statistical framework for determining time lags and estimating their uncertainties, including the full contributions from correlated noise, de-trending and interpolation. In essence, the lags are determined using a weighted average of all statistically acceptable models for interpolating the underlying *true* light curve. While we used the assumption that the underlying variable process had an exponential correlation function corresponding to a damped random walk, any other statistical process could be substituted. We note, however, that Kelly et al. (2009), Kozłowski et al. (2010) and MacLeod et al. (2010) have found the exponential correlation function to be an excellent model of quasar light curves, just as we have found here, although we modeled the light curves in flux rather than magnitude.

Because we are explicitly modeling the light curves, we must include an explicit model of the transfer function. Here we used a top hat for simplicity. It includes the simple limits of a delta function and a uniform thin shell, and is likely a reasonable model for any single-peaked transfer function given the available data (see Rybicki & Kleyna 1994). As with the model for the variability process, using an alternative transfer function simply requires computing the appropriate terms of the covariance matrix.

Aside from the case of NGC 7469 where it seemed to affect the lag estimation, we did not discuss the tophat width. In general, there is a relatively strong degeneracy between Δt, the width, and A, the scaling between the continuum and line light curves. When Δt is large and the continuum is heavily smoothed, the model will try to increase the variability amplitude by artificially boosting A to re-align the continuum and line light curves. However, the degeneracy does not seem to lead to problems in estimating the mean lag unless the line light curve is very poorly sampled. The traditional CCF method does not implicitly assume a shape for the transfer function but calculates the lag as either the barycenter (τ_{cent}) or the peak (τ_{peak}) of underlying transfer function (convolved with data). The difference between the two sometimes can be large and hard to reconcile unless the transfer function can be modeled explicitly. For future high-fidelity datasets, our approach should also have no difficulty constraining the shape of transfer functions.

The most important future path for this method is to simultaneously fit multiple line components, whether different lines (e.g., Hβ, Hα, etc.), velocity sub-components of individual lines or multiple continuum bands. As long as the overall *ansatz* that all light curves are scaled and smoothed versions of the continuum holds, combining many light curves with differing lags means that the lag estimate for any given light curve is now derived from a better sampled estimate of the continuum variability. A second advantage, particularly for attempts to study the velocity structure of a particular broad line, is that such joint analyses will correctly infer the covariances between the individual lags. Current velocity-dependent lags have uncertainties comparable to their differences (Bentz et al. 2008, 2010; Denney et al. 2009, 2010), but it may be true that these differences actually have a strong covariances, so that the differences are far more significant than estimates from analyzing the light curves in isolation. The method can also allow for luminosity-dependent lags or line-continuum scaling factors. Also note that while we only use the linear parameters of the model to remove the light curve means, it is a very flexible tool for de-trending or cross-calibrating light curves whose model uncertainties will be fully included in lag estimate.

The most important observational implication of this approach is the value of measuring multiple lines, especially those with high ionization potentials. In our approach, multiple lines with differing lags allow one to overcome many of the sampling problems inherent to cross-correlation methodologies. At its simplest, one light curve can be aliased into a (seasonal) sampling gap, but two cannot be unless the transfer functions are similar (i.e., the lines have similar lags). Given the radial

ionization stratification of the BLR (Peterson 1993), the lag difference between two lines is proportional to the difference in their ionization levels. In this paper, however, the lines we used for two-line fits are mostly pairs of two Balmer lines, which have similarly low ionization levels. Thus, the observational goal should be to obtain data for multiple lines with a broad range of ionization potentials. Indeed, with a wide variety of emission-line lines, it is in principle possible to combine the reverberation results with photoionization equilibrium modeling to highly constrain the geometry and physics of the BLR (Horne, Korista, & Goad 2003).

The only significant algorithmic challenge comes from the $\mathcal{O}(K^3)$ scaling of the computational cost with the number of data points K. Unfortunately, the reverberation mapping problem is very different from simply using the damped random walk to model the continuum light curves, where we can take advantage of the partic-ular structure of the covariance matrix to calculate the necessary matrix inversions in $\mathcal{O}(K)$ operations. Since the expensive matrix inversion is required for each likelihood calculation, it becomes difficult to analyze large data sets, particularly if the number of parameters also increases greatly as in a full simultaneous model of lags as a function of line velocity. These problems can be addressed using hyper–threaded or parallel versions of the underlying algorithm.

APPENDIX

COVARIANCE MATRIX OF THE CORRELATION FUNCTIONS

The expressions for the covariance matrices used in this paper and the accompanying code assume that the transfer function is a simple top hat,

$$\Psi(t - t') = A (t_2 - t_1)^{-1} \quad \text{for} \quad t_1 \leq t - t' \leq t_2. \tag{A1}$$

For this transfer function, we can analytically calculate the correlation functions in Equation (6), (7) and (8), respectively.

The Covariance Matrix Between the Continuum and One Line

The covariance between continuum $s_c(t)$ at t_j and line $s_l(t)$ at t_i with transfer function defined as in Equation (A1) is

$$\langle s_c(t_j) s_l(t_i) \rangle = \tau_d \sigma^2 A \begin{cases} e^{-t_L/\tau_d} - e^{-t_H/\tau_d} & \text{if } t_L > 0 \\ e^{t_H/\tau_d} - e^{t_L/\tau_d} & \text{if } t_H < 0 \\ 2 - e^{t_L/\tau_d} - e^{-t_H/\tau_d} & \text{if } t_L \leq 0 \leq t_H, \end{cases} \tag{A2}$$

where $t_L \equiv t_i - t_j - t_2$ and $t_H \equiv t_i - t_j - t_1$.

The Covariance Matrix Between Two Lines

Consider the case when the first line $s_l(t)$ has transfer function $\Psi(t - t')$ as defined in Equation (A1) and the other line $s_l'(t)$ has transfer function $\Psi'(t - t')$

$$\Psi'(t - t') = B (t_4 - t_3)^{-1} \quad \text{for} \quad t_3 \leq t - t' \leq t_4, \tag{A3}$$

where $t_4 - t_3 \leq t_2 - t_1$. The covariance between line $s_l(t)$ at time t_i and line $s_l'(t)$ at time t_j (Equation 8) is

$$\langle s_l(t_i) s_l'(t_j) \rangle = \tau_d^2 \sigma^2 A\, B \begin{cases} e^{-|t_L|/\tau_d} + e^{-|t_H|/\tau_d} - e^{-|t_{M1}|/\tau_d} - e^{-|t_{M2}|/\tau_d} + \begin{cases} 2\, t_H/\tau_d & \text{if } t_{M2} \leq 0 < t_H \\ 2\, (t_4 - t_3)/\tau_d & \text{if } t_{M2} \leq 0 < t_H \\ -2\, t_L/\tau_d & \text{if } t_L \leq 0 < t_{M1} \end{cases} \\ e^{-|t_L|/\tau_d} + e^{-|t_H|/\tau_d} - e^{-|t_{M1}|/\tau_d} - e^{-|t_{M2}|/\tau_d} \quad \text{if } t_L > 0 \text{ or } t_H < 0, \end{cases} \tag{A4}$$

where

$$\begin{aligned} t_L &\equiv (t_i - t_j) - (t_2 - t_3), \\ t_{M1} &\equiv (t_i - t_j) - (t_2 - t_3), \\ t_{M2} &\equiv (t_i - t_j) - (t_1 - t_3), \\ \text{and} \quad t_H &\equiv (t_i - t_j) - (t_1 - t_4). \end{aligned} \tag{A5}$$

By definition, the covariance for the autocorrelation of line $s_l(t)$ between time t_i and t_j (Equation 7) can be obtained by equating $\Psi'(t - t')$ with $\Psi(t - t')$ so that $B \equiv A$, $t_3 \equiv t_1$ and $t_4 \equiv t_2$.

REFERENCES

Alexander, T. 1997, in Astronomical Time Series, ed. Maoz, D., Sternberg, A., & Leibowitz, E. M. (Dordrecht: Kluwer), p. 163

Bentz, M. C., Peterson, B. M., Pogge, R. W., Vestergaard, M., & Onken, C. A. 2006, ApJ, 644, 133

Bentz, M. C., et al. 2006, ApJ, 651, 775
Bentz, M. C., et al. 2007, ApJ, 662, 205
Bentz, M. C., et al. 2008, ApJ, 689, L21
Bentz, M. C., Peterson, B. M., Pogge, R. W., & Vestergaard, M. 2009, ApJ, 694, L166
Bentz, M. C., Peterson, B. M., Netzer, H., Pogge, R. W., & Vestergaard, M. 2009, ApJ, 697, 160
Bentz, M. C., et al. 2010, ApJ, 720, 46
Blandford, R. D., & McKee, C. F. 1982, ApJ, 255, 419
Cackett, E. M., & Horne, K. 2006, MNRAS, 365, 1180
Clavel, J., et al. 1991, ApJ, 366, 64
Collier, S., & Peterson, B. M. 2001, ApJ, 555, 775
Collier, S. J., et al. 1998, ApJ, 500, 162
Denney, K. D., et al. 2006, ApJ, 653, 152
Denney, K. D., et al. 2009, ApJ, 704, L80
Denney, K. D., et al. 2010, ApJ, 721, 715
Edelson, R. A., & Krolik, J. H. 1988, ApJ, 333, 646
Ferrarese, L., & Merritt, D. 2000, ApJ, 539, L9
Ferrarese, L., Pogge, R. W., Peterson, B. M., Merritt, D., Wandel, A., & Joseph, C. L. 2001, ApJ, 555, L79
Gaskell, C. M., & Sparke, L. S. 1986, ApJ, 305, 175
Gaskell, C. M., & Peterson, B. M. 1987, ApJS, 65, 1
Gebhardt, K., et al. 2000, ApJ, 539, L13
Gebhardt, K., et al. 2000, ApJ, 543, L5
Graham, A.W., Onken, C.A., Athanassoula, E. & Combes, F. 2011, submitted to MNRAS (arXiv:1007.3834)
Grier, C. J., et al. 2008, ApJ, 688, 837
Gültekin, K., et al. 2009, ApJ, 698, 198
Hastings, W. K. 1970, Biometrika, 57, 97
Hopkins, P. F., & Hernquist, L. 2006, ApJS, 166, 1
Horne, K., Korista, K. T., & Goad, M. R. 2003, MNRAS, 339, 367
Horne, K., Peterson, B. M., Collier, S. J., & Netzer, H. 2004, PASP, 116, 465
Kaspi, S., Smith, P. S., Maoz, D., Netzer, H., & Jannuzi, B. T. 1996, ApJ, 471, L75
Kaspi, S., Smith, P. S., Netzer, H., Maoz, D., Jannuzi, B. T., & Giveon, U. 2000, ApJ, 533, 631
Kaspi, S., Maoz, D, Netzer, H., Peterson, B.M., Vestergaard, M., Jannuzi, B.T. 2005, ApJ, 629, 61
Kelly, B. C., Bechtold, J., & Siemiginowska, A. 2009, ApJ, 698, 895
Kelly, B. C., Vestergaard, M., Fan, X., Hopkins, P., Hernquist, L., & Siemiginowska, A. 2010, ApJ, 719, 1315
Kollmeier, J. A., et al. 2006, ApJ, 648, 128
Kozłowski, S., & Kochanek, C. S. 2009, ApJ, 701, 508
Kozłowski, S., et al. 2010, ApJ, 708, 927
Korista, K. T., & Goad, M. R. 2004, ApJ, 606, 749
Kormendy, J., & Richstone, D. 1995, ARA&A, 33, 581
Krolik, J. H. 1999, Active Galactic Nuclei: From the Central Black Hole to the Galactic Environment (Princeton , N. J.: Princeton University Press)
Krolik, J. H., Horne, K., Kallman, T. R., Malkan, M. A., Edelson, R. A., & Kriss, G. A. 1991, ApJ, 371, 541
Labita, M., Treves, A., Falomo, R., & Uslenghi, M. 2006, MNRAS, 373, 551
MacLeod, C. L., et al. 2010, ApJ, 721, 1014
Magorrian, J., et al. 1998, AJ, 115, 2285
Marconi, A., Axon, D. J., Maiolino, R., Nagao, T., Pastorini, G., Pietrini, P., Robinson, A., & Torricelli, G. 2008, ApJ, 678, 693

Marconi, A., Axon, D. J., Maiolino, R., Nagao, T., Pietrini, P., Risaliti, G., Robinson, A., & Torricelli, G. 2009, ApJ, 698, L103
McLure, R. J., & Jarvis, M. J. 2002, MNRAS, 337, 109
McLure, R. J., & Jarvis, M. J. 2004, MNRAS, 353, L45
Metropolis, N., Rosenbluth, A. W., Rosenbluth, M. N., Teller, A. H., & Teller, E. 1953, J. Chem. Phys., 21, 1087
Nelson, C. H., Green, R. F., Bower, G., Gebhardt, K., & Weistrop, D. 2004, ApJ, 615, 652
Netzer, H., & Marziani, P. 2010, ApJ, 724, 318
Netzer, H. 2009, ApJ, 695, 793
Osterbrock, D. E. 1989, Astrophysics of Gaseous Nebulae and Active Galactic Nuclei (Mill Valley CA: University Science Books)
Onken, C. A., Ferrarese, L., Merritt, D., Peterson, B. M., Pogge, R. W., Vestergaard, M., & Wandel, A. 2004, ApJ, 615, 645
Peng, C. Y., Impey, C. D., Ho, L. C., Barton, E. J., & Rix, H.-W. 2006, ApJ, 640, 114
Peterson, B. M. 1993, PASP, 105, 247
Peterson, B. M. 1997, An Introduction to Active Galactic Nuclei, (Cambridge: Cambridge University Press)
Peterson, B. M., & Wandel, A. 1999, ApJ, 521, L95
Peterson, B. M., & Wandel, A. 2000, ApJ, 540, L13
Peterson, B. M. 2001, Advanced Lectures on the Starburst-AGN Connection, ed. I. Aretxaga, D. Kunth, & R. Mújica (Singapore: World Scientific), p.3
Peterson, B. M. 2008, New Astronomy Review, 52, 240
Peterson, B. M., et al. 1991, ApJ, 368, 119
Peterson, B. M., Wanders, I., Bertram, R., Hunley, J. F., Pogge, R. W., & Wagner, R. M. 1998, ApJ, 501, 82
Peterson, B. M., et al. 2004, ApJ, 613, 682
Press, W. H., Rybicki, G. B., & Hewitt, J. N. 1992, ApJ, 385, 404
Press, W. H., Teukolsky, S. A., Vetterling, W. T., & Flannery, B. P. 1992, Numerical Recipes in FORTRAN. The Art of Scientific Computing, (Cambridge: Cambridge University Press)
Rauch, K. P., & Blandford, R. D. 1991, ApJ, 381, L39
Rybicki, G. B., & Kleyna, J. T. 1994, in ASP Conf. Ser. 69, Reverberation Mapping of the Broad-Line Region in Active Galactic Nuclei, ed. P. M. Gondhalekar, K. Horne, & B. M. Peterson (San Francisco: ASP), p. 85
Rybicki, G. B., & Press, W. H. 1992, ApJ, 398, 169
—. 1995, Physical Review Letters, 74, 1060
Steinhardt, C. L., & Elvis, M. 2010, MNRAS, 402, 2637
Shankar, F., Weinberg, D. H., & Miralda-Escudé, J. 2009, ApJ, 690, 20
Shen, Y., Greene, J. E., Strauss, M. A., Richards, G. T., & Schneider, D.P. 2008, ApJ, 680, 169
Tremaine, S., et al. 2002, ApJ, 574, 740
Udalski, A., Szymanski, M. K., Soszynski, I., & Poleski, R. 2008, Acta Astronomica, 58, 69
Vestergaard, M. 2002, ApJ, 571, 733
Vestergaard, M., & Peterson, B. M. 2006, ApJ, 641, 689
Wandel, A., Peterson, B. M., & Malkan, M. A. 1999, ApJ, 526, 579
Wanders, I., et al. 1993, A&A, 269, 39
Wambsganss, J. 2006, Gravitational Lensing: Strong, Weak and Micro, Saas-Fee Advanced Courses, Volume 33. (Berlin: Springer-Verlag) p. 453
Welsh, W. F. 1999, PASP, 111, 1347
White, R. J., & Peterson, B. M. 1994, PASP, 106, 879
Woo, J.-H., et al. 2010, ApJ, 716, 269